Tamás Szidarovszky

Rovibrational spectra near dissociation

Supervisor:

Prof. Dr. Attila G. Császár

Laboratory of Molecular Structure and Dynamics, Institute of Chemistry

Eötvös University

Chemistry Doctoral School

Head of the doctoral school: Prof. Dr. György Inzelt

Theoretical and Physical Chemistry, Structural Chemistry Doctoral Programme

Head of the doctoral programme: Prof. Dr. Péter Surján

Eötvös University

Budapest, 2012

CONTENTS

I. INTRODUCTION 5

II. COMPUTING (RO)VIBRATIONAL STATES UP TO DISSOCIATION 7

II.1. Computation of bound rovibrational states 8
II.1.1. Hamiltonian in the R_1 embedding 8
II.1.2. Matrix representation in the R_1 embedding 9
II.1.3. Symmetry considerations 12
II.1.4. Applications 13
II.1.4.1. High accuracy vibrational energy levels of H_2O up to near dissociation 13
II.1.4.2. High accuracy rovibrational energy levels of H_3^+ and its isotopologues H_2D^+ and D_2H^+ 14
II.1.5. Concluding remarks 17

II.2. Assigning approximate quantum numbers 18
II.2.1. Theoretical background of the rigid rotor decomposition (RRD) scheme 18
II.2.2. The RRD package for D^2FOPI 19
II.2.3. Embedding dependence of the RRD 20
II.2.3.1. Computational details 21
II.2.3.2. Embedding, energy, and J dependence of the RRD scheme 22
II.2.4. Validation of quantum labels for H_2O, comparison with the BT2 linelist 26
II.2.5. Validation of quantum labels for H_2D^+ and D_2H^+ 27
II.2.6. Concluding remarks 31

II.3. On the DVR of essential singularities 32
II.3.1. The case of a complete basis set 32
II.3.2. The case of incomplete basis sets 33
II.3.3. Test computations 34

III. ENERGY LEVELS BEYOND DISSOCIATION 38

III.1. What are resonance states? 38

III.2. Computing resonance states in quantum chemistry 42
III.2.1. Complex Absorbing Potential (CAP) method 42
III.2.2. D^2FOPI and the CAP method 44
III.2.3. Complex coordinate scaling 45
III.2.3.1. What is complex scaling? 45
III.2.3.2. Effect of complex scaling on the asymptotic behavior of wave functions 46
III.2.3.3. The complex scaled Hamiltonian 48
III.2.3.4. Detecting resonance eigenstates in the complex coordinate formalism 49
III.2.4. D^2FOPI and the complex coordinate method 50

III.3. Applications 52
III.3.1. One-dimensional tests 52
III.3.2. Resonance states of H_2O 58
III.3.3. Resonance states of H_3^+ 63

IV. SUMMARY 67

V. ACKNOWLEDGEMENTS 69

I. Introduction

During the past one hundred years, spectroscopy has been one of the most important experimental tools to obtain information about and understand atomic and molecular phenomena. Cooperation between theory and experiment led to the development and refinement of theoretical models and to an understanding of interactions and dynamics of molecules. Furthermore, spectroscopy proved to an excellent tool for analytic and structural analyses. In spite of the long history of the development of molecular spectroscopy, there are many open questions and challenges that remain. One of these, providing one of the principal motivations for the present work, is an improved understanding and modeling of an exotic molecular phenomenon, (ro)vibrational resonances (also known as quasi-bound states). Resonances have energies higher than the first dissociation limit. Understanding how molecules behave around the point of dissociation is fundamental to several points of chemistry, as chemical reactions by definition involve bond breaking and bond making.

Measuring transitions corresponding to (ro)vibrational resonance states is a complex task; nonetheless, there are experimental data available. In fact the famous Carrington pre-dissociation spectrum[1,2] of the H_3^+ molecule is characterized by a large number of lines associated with resonance states. Assigning this spectrum is one of the longest-running unsolved problems of molecular spectroscopy. Furthermore, detailed knowledge of the spectroscopy of H_3^+ is important on its own right, since although under terrestrial conditions H_3^+ does not exist due to the low proton affinity of the H_2 molecule, H_3^+ is an important interstellar molecule, and also a dominant ion in cool hydrogen plasmas. H_3^+ is also the simplest polyatomic molecule having just two electrons and three nuclei; thus, it can also serve as a benchmark system for methodological developments aimed at high accuracy.

Another unquestionably important molecule with experimentally available resonance states is the water molecule. The resonance states of H_2O have been investigated via state-selective, triple-resonance spectroscopy by Grechko et. al.[3] Unlike the Carrington bands for H_3^+, which are extremely dense and have hundreds of lines per one wavenumber, the resonance lines in the spectra of water obtained with state-selective spectroscopy are much sparser and have experimentally determined quantum numbers based on selection rules, which makes their theoretical interpretation much easier.

In order to reach the goal of computing exotic (ro)vibrational resonance states and to understand near-dissociation spectra, one must be able to compute all the bound states below

dissociation. Even for triatomic molecules this task requires an immense amount of computational work both in electronic structure and nuclear motion theory, despite the developments in computational quantum chemistry.

To construct a potential energy surface (PES) which has global spectroscopic accuracy all the way to the first dissociation limit is by itself a significant challenge. This has been achieved for only a few molecules. Without going into details, only two issues are noted. The first difficulty in constructing a PES having correct dissociative behavior is the computation of the great many accurate energy values near dissociation, where usually several electronic states get close to each other. Therefore, one needs to consider multireference methods along with adiabatic corrections. Even if one is capable of producing the large number of accurate PES points which cover the coordinate space sufficiently densely, a second difficulty arises, namely the fitting of an analytical functional form to the energy points in the asymptotic region with high accuracy.

If an accurate global PES is at hand, computation of the bound rovibrational states up to dissociation can be attempted. Although in principle this task is straightforward, it is far from being trivial. In order to compute the many (hundreds or thousands of) bound states, one needs to use an effective algorithm which is capable of describing the diffuse, highly excited states. This requires a compact basis set expansion of the wavefunction, which can be achieved most straightforwardly using internal coordinates with corresponding prederived, tailor-made Hamiltonians.[4] However, such operators always contain singular terms which might diverge at some coordinate values. If these so-called singular nuclear configurations, corresponding to singularities present in the kinetic energy operator, are energetically accessible by the nuclear motions investigated, special care must be exercised to avoid the resulting numerical problems during variational computation of (ro)vibrational energy levels. Theoretical techniques that do not treat these singularities may result in unconverged eigenenergies; therefore, these methods cannot be employed when the goal is the determination of the complete (ro)vibrational spectrum.

Due partly to the lack of accurate global PESs for molecules beyond three atoms at present, my work of methodology development was dedicated to triatomic systems. The goal was to develop an effective algorithm and a corresponding computer code which are capable of determining bound states of triatomic molecules up to and beyond the first dissociation asymptote. While on route to achieve this goal, the need to extend the algorithm with a

rovibrational quantum number labeling protocol and to investigate in detail the effect of the singularities of the Hamiltonian in the computational methods implemented arose.

Following this train of thought, the first half of my thesis deals with the highly efficient D^{2}FOPI protocol [5] (*mixed Discrete variable (DVR) [6] and Finite basis (FBR)[6] representation of the rovibrational Hamiltonian expressed in Orthogonal internal coordinates using a direct Product basis set and an Iterative eigensolver*) developed for bound state (ro)vibrational computations, along with sections on some relevant applications. This is followed by sections about the implementation of the rovibrational quantum number labeling protocol and its use in spectroscopic applications. Finally, the first half of the thesis is concluded with the summary of the current knowledge on the effects and the surprising lack of effects of the singular operator terms in certain grid-based computational methods.

The second half of the thesis is dedicated to the computation of (ro)vibrational resonance states. After an introduction to resonance states, the possible algorithms for their determination using quantum chemical techniques are discussed along with merging of these algorithms with the D^{2}FOPI protocol. Following are the sections on applications about one- and three-dimensional vibrational resonance computations.

The thesis ends with the summary of the work done.

II. Computing (ro)vibrational states up to dissociation

As mentioned in the Introduction, in order to compute (ro)vibrational resonance states in a time-independent formalism based on bound-state methodologies (see details in section III.2.), one needs a computational method capable of determining (ro)vibrational eigenstates all the way to dissociation. This section demonstrates the virtues of the current version of the highly efficient rovibrational D^{2}FOPI protocol and code. The D^{2}FOPI algorithm used to be able to treat only molecular vibrations. It was extended during my PhD work so it can now deal with rovibrational problems, as well.

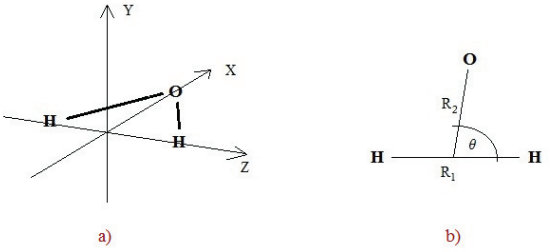

Figure. 1.

a) a possible R_1 embedding of the body fixed coordinate frame for water molecule using b) Jacobi coordinates

II.1. Computation of bound rovibrational states

The particular form of the Sutcliffe–Tennyson rovibrational Hamiltonian[4] of triatomic molecules utilized in the D^{2}FOPI protocol is based on orthogonal internal coordinates $\{R_1,R_2,\Theta\}$. These can be, for example, Jacobi[7] or Radau[8] coordinates, while the embedding of the body-fixed coordinate frame can either be the R_1[9] or the bisector[10] embedding. To avoid the discussion being unnecessarily long, only the case of using the R_1 embedding is discussed in detail below, as the R_1 embedding was favored in most applications presented in this thesis. See Fig. 1 for an example of a possible definition of the Jacobi coordinates R_1, R_2, and Θ in the R_1 embedding for the case of the water molecule.

II.1.1. Hamiltonian in the R_1 embedding

For $J = 0$ the Hamiltonian in atomic units reads, as

$$\hat{H} = -\frac{1}{2\mu_1}\frac{\partial^2}{\partial R_1^2} - \frac{1}{2\mu_2}\frac{\partial^2}{\partial R_2^2} - \left(\frac{1}{2\mu_1 R_1^2} + \frac{1}{2\mu_2 R_2^2}\right)\left(\frac{\partial^2}{\partial \Theta^2} + \cot\Theta\frac{\partial}{\partial \Theta}\right) + \hat{V}\left(R_1, R_2, \Theta\right). \qquad (1)$$

In the R_1 embedding, whereby the z axis of the body-fixed frame is chosen to lie parallel to the interatomic vector described by the R_1 coordinate, the Hamiltonian in atomic units for $J > 0$ reads, as

$$\hat{H} = -\frac{1}{2\mu_1}\frac{\partial^2}{\partial R_1^2} - \frac{1}{2\mu_2}\frac{\partial^2}{\partial R_2^2} - \left(\frac{1}{2\mu_1 R_1^2} + \frac{1}{2\mu_2 R_2^2}\right)\left(\frac{\partial^2}{\partial \Theta^2} + \cot\Theta\frac{\partial}{\partial \Theta} - \frac{\hat{j}_z^2}{\sin^2\Theta}\right), \quad (2)$$
$$+\frac{1}{2\mu_1 R_1^2}\left(\hat{J}^2 - 2\hat{J}_z\hat{j}_z - \hat{J}_+\hat{j}_- - \hat{J}_-\hat{j}_+\right) + \hat{V}\left(R_1, R_2, \Theta\right).$$

In these expressions $\hat{V}$ is the potential energy operator, μ_1 and μ_2 are appropriately defined[4] mass-dependent constants, R_1 and R_2 denote the two stretching-type coordinates, Θ is a bending-type coordinate, $\hat{J}$ and $\hat{j}$ refer to the appropiate rotational angular momenta, and the volume element for integration is $\sin\varphi\sin\Theta d\chi d\psi d\varphi dR_1 dR_2 d\Theta$ with φ, χ and ψ being the coordinates corresponding to the overall rotation of the molecule. It is noted that the above forms of the Hamiltonians in Eqs. (1) and (2) are obtained by merging the stretching coordinate dependent parts of the volume element of integration into the Hamiltonians. This in turn means that the computed eigenfunctions of the Hamiltonians are the physical wave functions multiplied by the stretching type coordinates.

II.1.2. Matrix representation in the R_1 embedding

The D^{2}FOPI approach utilizes an orthogonal and normalized product basis of the form $\left\{\chi_{n_1}(R_1)\chi_{n_2}(R_2)P_l^K(\cos\Theta)C_{MK}^{Jp}(\varphi,\chi,\psi)\right\}_{n_1=1,n_2=1,K=p,J=K}^{N_1,\ N_2,\ J,\ K+N_L-1}$, where the $\chi_{n_1}(R_1)$ and $\chi_{n_2}(R_2)$ functions are DVR functions, $P_l^K(\cos\Theta)$ is the lth normalized associated Legendre function, $C_{MK}^{Jp}(\varphi,\chi,\psi)$ are symmetry-adapted rotational functions of the form

$$C_{MK}^{Jp}(\varphi,\chi,\psi) = \left[2\left(1+\delta_{K0}\right)\right]^{-1/2}\left[D_{MK}^{J} + (-1)^p D_{M-K}^{J}\right],\ p\in\{0,1\}, K\in\{p, p+1, ..., J-1, J\} \quad (3)$$

where p stands for parity,[11] M and K are the usual quantum numbers corresponding to space- and body-fixed projections of the rotational angular momentum on the appropriate z axis, and D_{MK}^{J} are the normalized Wigner rotation functions.[11]

Due to the „almost" direct-product nature of the basis set (almost refers to the coupling between the $P_l^K(\cos\Theta)$ Legendre polynomials and the $C_{MK}^{Jp}(\varphi,\chi,\psi)$ rotation functions via K), the matrix representation of the triatomic Hamiltonian of Eqs. (1) and (2) can be written as a sum of direct-product matrices, which takes the following form in the R_1 embedding, after performing the integration over the rotational coordinates:

$$\mathbf{H}_{\text{vib}} = \mathbf{K}_1^{N_1\times N_1}\otimes\mathbf{I}^{N_2\times N_2}\otimes\mathbf{I}^{N_L\times N_L} + \mathbf{I}^{N_1\times N_1}\otimes\mathbf{K}_2^{N_2\times N_2}\otimes\mathbf{I}^{N_L\times N_L} +$$
$$+\mathbf{R}_1^{N_1\times N_1}\otimes\mathbf{I}^{N_2\times N_2}\otimes\mathbf{K}_\Theta^{N_L\times N_L} + \mathbf{I}^{N_1\times N_1}\otimes\mathbf{R}_2^{N_2\times N_2}\otimes\mathbf{K}_\Theta^{N_L\times N_L} + \mathbf{V}_{\text{vib}} \quad (4)$$

for $J = 0$, and

$$\begin{aligned}\mathbf{H}_{\text{rovib}} &= \mathbf{I}^{K_{\max}\times K_{\max}} \otimes \mathbf{K}_1^{N_1\times N_1} \otimes \mathbf{I}^{N_2\times N_2} \otimes \mathbf{I}^{N_L\times N_L} + \mathbf{I}^{K_{\max}\times K_{\max}} \otimes \mathbf{I}^{N_1\times N_1} \otimes \mathbf{K}_2^{N_2\times N_2} \otimes \mathbf{I}^{N_L\times N_L} + \\ &+ \sum_{K=p}^{J}\Big[\mathbf{E}_{K,K}^{K_{\max}\times K_{\max}} \otimes \mathbf{R}_1^{N_1\times N_1} \otimes \mathbf{I}^{N_2\times N_2} \otimes \mathbf{K}_\Theta^{K,N_L\times N_L} + \mathbf{E}_{K,K}^{K_{\max}\times K_{\max}} \otimes \mathbf{I}^{N_1\times N_1} \otimes \mathbf{R}_2^{N_2\times N_2} \otimes \mathbf{K}_\Theta^{K,N_L\times N_L} + \\ &+ \mathbf{E}_{K,K+1}^{K_{\max}\times K_{\max}} \otimes \mathbf{R}_1^{N_1\times N_1} \otimes \mathbf{I}^{N_2\times N_2} \otimes \mathbf{B}_K^{+} + \mathbf{E}_{K,K-1}^{K_{\max}\times K_{\max}} \otimes \mathbf{R}_1^{N_1\times N_1} \otimes \mathbf{I}^{N_2\times N_2} \otimes \mathbf{B}_K^{-}\Big] + \\ &+ \mathbf{E}_{K,K}^{K_{\max}\times K_{\max}} \otimes \widetilde{\mathbf{R}}_1^{K,N_1\times N_1} \otimes \mathbf{I}^{N_2\times N_2} \otimes \mathbf{I}^{N_L\times N_L} + \mathbf{V}_{\text{rovib}}\end{aligned} \tag{5}$$

for $J > 0$, where

$$\begin{aligned}&\left(\mathbf{K}_j^{N_j\times N_j}\right)_{n_j,n_j'} = \left\langle \chi_{n_j}(R_j)\middle| -\frac{1}{2\mu_j}\frac{\partial^2}{\partial R_j^2}\middle|\chi_{n_j'}(R_j)\right\rangle \quad j = 1 \text{ or } 2,\\ &\left(\mathbf{R}_j^{N_j\times N_j}\right)_{n_j,n_j'} = \left\langle \chi_{n_j}(R_j)\middle|\frac{1}{2\mu_j R_j^2}\middle|\chi_{n_j'}(R_j)\right\rangle \quad j = 1 \text{ or } 2,\\ &\left(\mathbf{K}_\Theta^{N_L\times N_L}\right)_{\ell,\ell'} = \left\langle P_l^0(\cos\Theta)\middle| -\left(\frac{\partial^2}{\partial\Theta^2} + \cot\Theta\frac{\partial}{\partial\Theta}\right)\middle| P_{l'}^0(\cos\Theta)\right\rangle,\\ &\left(\mathbf{K}_\Theta^{K,N_L\times N_L}\right)_{\ell,\ell'} = \left\langle P_l^K(\cos\Theta)\middle| -\left(\frac{\partial^2}{\partial\Theta^2} + \cot\Theta\frac{\partial}{\partial\Theta} - \frac{\hat{j}_z^2}{\sin^2\Theta}\right)\middle| P_{l'}^K(\cos\Theta)\right\rangle\\ &\widetilde{\mathbf{R}}_1^{K,N_1\times N_1} = \left[J(J+1) - 2K^2\right]\cdot\mathbf{R}_1^{N_1\times N_1},\end{aligned} \tag{6}$$

and the matrices $\mathbf{I}^{\alpha\times\alpha}$ are $\alpha\times\alpha$-dimensional unit matrices, the matrices $\mathbf{E}_{\alpha,\beta}^{K_{\max}\times K_{\max}}$ have only one non-zero element equal to one at the indicated subscripts, $\left(\mathbf{B}_K^{\pm}\right)_{l,l'} = -\delta_{l,l'\pm1}\left(1+\delta_{K,0}+\delta_{K',0}\right)^{1/2}\Lambda_{lK}^{\pm}\Lambda_{l'K}^{\pm}$, where $\Lambda_{\alpha K}^{\pm} = \sqrt{\alpha(\alpha+1) - K(K\pm1)}$, and the elements of the potential energy matrix are

$$\left(\mathbf{V}_{\text{vib}}\right)_{n_1n_2\ell,n_1'n_2'\ell'} = \left\langle \chi_{n_1}(R_1)\chi_{n_2}(R_2)\Phi_\ell(\cos\Theta)\middle|V(R_1,R_2,\cos\Theta)\middle|\chi_{n_1'}(R_1)\chi_{n_2'}(R_2)\Phi_{\ell'}(\cos\Theta)\right\rangle \tag{7}$$

for $J = 0$ and

$$\begin{aligned}&\left(\mathbf{V}_{\text{rovib}}\right)_{n_1n_2\ell K,n_1'n_2'\ell'K'} =\\ &\delta_{K,K'}\left\langle \chi_{n_1}(R_1)\chi_{n_2}(R_2)\Phi_l^K(\cos\Theta)\middle|V(R_1,R_2,\cos\Theta)\middle|\chi_{n_1'}(R_1)\chi_{n_2'}(R_2)\Phi_{l'}^{K'}(\cos\Theta)\right\rangle\end{aligned} \tag{8}$$

for $J > 0$.

In order to have a compact basis expansion, in the D^{2}FOPI program $\chi_{n_1}(R_1)$ and $\chi_{n_2}(R_2)$ can be chosen to be "potential optimized" (PO) DVR functions,[12-14] *i.e.*, DVR functions obtained from the eigenfunctions of the 1D effective Hamiltonian

$\hat{H}_j^{\rm 1D} = -\frac{1}{2\mu_j}\frac{d^2}{dR_j^2} + \hat{V}\left(R_j;R_{j'},\Theta\right)$, j, j' = 1, 2 or 2, 1 with $\hat{V}\left(R_j;R_{j'},\Theta\right)$ chosen to be a relaxed 1D potential, *i.e.*, $\hat{V}\left(R_j;R_{j'},\Theta\right)$ is obtained by optimizing the $R_{j'}$ and Θ coordinates for each value of R_j.

It is worth making the following three comments. (1) Since in the D^{2}FOPI computations the distance-dependent basis functions are chosen to be DVR functions, the potential energy matrix is diagonal in the corresponding n_1 and n_2 indices, therefore it has a block-diagonal structure. (2) The Legendre polynomials $P_l^0(\cos\Theta)$, $l \in \{0,1,...,N_L\}$ and $P_l^K(\cos\Theta)$, $l \in \{K, K+1,..., K+N_L-1\}$ are eigenfunctions of the Θ -dependent $-\left(\frac{\partial^2}{\partial\Theta^2} + \cot\Theta\frac{\partial}{\partial\Theta}\right)$ and $-\left(\frac{\partial^2}{\partial\Theta^2} + \cot\Theta\frac{\partial}{\partial\Theta} - \frac{\hat{j}_z^2}{\sin^2\Theta}\right)$ operators [see Eqs.(6)], respectively, with eigenvalues $l(l+1)$. (3) In the R_1 embedding the matrices $\mathbf{R}_j^{N_j\times N_j}$ (j = 1 or 2) can chosen to be calculated by the exact-DVR method for treating the singularities,[5] therefore, seize to be diagonal. This, however, does not change the structure of the Hamiltonian matrix, while the same terms present in the bisector embedding are diagonal (using the exact-DVR method here would lead to a much more dense Hamiltonian matrix). Taking (1), (2), and (3) into account, an element of the $N_1N_2N_L\times N_1N_2N_L$-dimensional $\mathbf{H}_{\rm vib}$ matrix in the R_1 embedding can be written as

$$\begin{aligned}
\left(\mathbf{H}_{\rm vib}\right)_{n_1n_2l,n_1'n_2'l'} &= \delta_{n_2,n_2'}\delta_{l,l'}\left(\mathbf{K}_1^{N_1\times N_1}\right)_{n_1,n_1'} + \delta_{n_1,n_1'}\delta_{l,l'}\left(\mathbf{K}_2^{N_2\times N_2}\right)_{n_2,n_2'} + \\
&+ \delta_{n_2,n_2'}\left(\mathbf{R}_1^{N_1\times N_1}\right)_{n_1,n_1'}\left(\mathbf{K}_\Theta^{N_L\times N_L}\right)_{l,l'} + \delta_{n_1,n_1'}\left(\mathbf{R}_2^{N_2\times N_2}\right)_{n_2,n_2'}\left(\mathbf{K}_\Theta^{N_L\times N_L}\right)_{l,l'} + \left(\mathbf{V}_{vib}\right)_{n_1n_2l,n_1'n_2'l'} = \\
&= \delta_{n_2,n_2'}\delta_{l,l'}\left(\mathbf{K}_1^{N_1\times N_1}\right)_{n_1,n_1'} + \delta_{n_1,n_1'}\delta_{l,l'}\left(\mathbf{K}_2^{N_2\times N_2}\right)_{n_2,n_2'} + \delta_{n_2,n_2'}\delta_{l,l'}l\left(l+1\right)\left(\mathbf{R}_1^{N_1\times N_1}\right)_{n_1,n_1'} + \\
&+ \delta_{n_1,n_1'}\delta_{l,l'}l\left(l+1\right)\left(\mathbf{R}_2^{N_2\times N_2}\right)_{n_2,n_2'} + \delta_{n_1,n_1'}\delta_{n_2,n_2'}\left\langle P_l^0(\cos\Theta)\middle|V(q_{n_1},q_{n_2},\cos\Theta)\middle|P_{l'}^0(\cos\Theta)\right\rangle
\end{aligned}, \qquad (9)$$

while an element of the $N_1N_2N_LK_{\max}\times N_1N_2N_LK_{\max}$-dimensional $\left(K_{\max} = J+1-p\right)$ $\mathbf{H}_{\rm rovib}$ matrix with given J and p can be written as

$$
\begin{aligned}
\left(\mathbf{H}_{\text{rovib}}\right)_{Kn_1n_2l,K'n_1'n_2'l'} &= \delta_{K,K'}\delta_{n_2,n_2'}\delta_{l,l'}\left(\mathbf{K}_1^{N_1\times N_1}\right)_{n_1,n_1'} + \delta_{n_1,n_1'}\delta_{l,l'}\left(\mathbf{K}_2^{N_2\times N_2}\right)_{n_2,n_2'} + \\
&+ \delta_{K,K'}\delta_{n_2,n_2'}\left(\mathbf{R}_1^{N_1\times N_1}\right)_{n_1,n_1'}\left(\mathbf{K}_\Theta^{N_L\times N_L}\right)_{l,l'} + \delta_{K,K'}\delta_{n_1,n_1'}\left(\mathbf{R}_2^{N_2\times N_2}\right)_{n_2,n_2'}\left(\mathbf{K}_\Theta^{N_L\times N_L}\right)_{l,l'} + \\
&+ \delta_{K,K'-1}\delta_{n_2,n_2'}\left(\mathbf{R}_1^{N_1\times N_1}\right)_{n_1,n_1'}\left(\mathbf{B}_K^{+}\right)_{l,l'} + \delta_{K,K'+1}\delta_{n_2,n_2'}\left(\mathbf{R}_1^{N_1\times N_1}\right)_{n_1,n_1'}\left(\mathbf{B}_K^{-}\right)_{l,l'} + \\
&+ \delta_{K,K'}\delta_{n_2,n_2'}\delta_{l,l'}\left(\tilde{\mathbf{R}}_1^{K,N_1\times N_1}\right)_{n_1,n_1'} + \delta_{K,K'}\left(\mathbf{V}_{rovib}\right)_{n_1n_2l,n_1'n_2'l'} = \\
&= \delta_{K,K'}\delta_{n_2,n_2'}\delta_{l,l'}\left(\mathbf{K}_1^{N_1\times N_1}\right)_{n_1,n_1'} + \delta_{n_1,n_1'}\delta_{l,l'}\left(\mathbf{K}_2^{N_2\times N_2}\right)_{n_2,n_2'} + \\
&+ \delta_{K,K'}\delta_{n_2,n_2'}\delta_{l,l'}(l+K)(l+K-1)\left(\mathbf{R}_1^{N_1\times N_1}\right)_{n_1,n_1'} + \\
&+ \delta_{K,K'}\delta_{n_1,n_1'}\delta_{l,l'}(l+K)(l+K-1)\left(\mathbf{R}_2^{N_2\times N_2}\right)_{n_2,n_2'} - \\
&- \delta_{K,K'-1}\delta_{n_2,n_2'}\delta_{l,l'+1}\left(1+\delta_{K,0}+\delta_{K',0}\right)^{1/2}\Lambda_{JK}^{+}\Lambda_{IK}^{+}\left(\mathbf{R}_1^{N_1\times N_1}\right)_{n_1,n_1'} - \\
&- \delta_{K,K'+1}\delta_{n_2,n_2'}\delta_{l,l'-1}\left(1+\delta_{K,0}+\delta_{K',0}\right)^{1/2}\Lambda_{JK}^{-}\Lambda_{IK}^{-}\left(\mathbf{R}_1^{N_1\times N_1}\right)_{n_1,n_1'} + \\
&+ \delta_{K,K'}\delta_{n_2,n_2'}\delta_{l,l'}\left[J(J+1)-2K^2\right]\left(\mathbf{R}_1^{N_1\times N_1}\right)_{n_1,n_1'} + \\
&+ \delta_{K,K'}\delta_{n_1,n_1'}\delta_{n_2,n_2'}\left\langle P_l^K\left(\cos\Theta\right)\middle|V(q_{n_1},q_{n_2},\cos\Theta)\middle|P_{l'}^{K'}\left(\cos\Theta\right)\right\rangle
\end{aligned}
\tag{10}
$$

where q_{n_1} and q_{n_2} are the n_1th and n_2th DVR points of the R_1 and R_2 coordinates, respectively. One can see from the above formulae that the matrix representation of the Hamiltonian has a very sparse and a priori known structure. This makes the use of an iterative eigensolver, *e.g.*, the Lánczos algorithm,[15-17] straightforward for obtaining the required eigenpairs.

II.1.3. Symmetry considerations

It should be noted that apart form the use of symmetrized rotational basis functions for $J \neq 0$ calculations, symmetry can be exploited for the $J = 0$ case also for systems of the AX_2 type. Computations within D^{2}FOPI using the Jacobi or Radau coordinate systems in principle could be separated into two symmetry blocks by symmetry adopting the bending and the stretching type basis functions, respectively. So far the symmetrization is implemented only in Jacobi coordinates, which is straightforward when using Legendre basis, since the only term in the vibrational Hamiltonain matrix not diagonal in the Legendre basis indices is the last term in Eq. (9). This term can be separated into two blocks by realizing that it is zero if the two Legendre functions in the term have different parity. The reason for this is that the potential energy function is an even function of the $\cos\Theta$ coordinate, and when multiplied by Legendre functions of different, *i.e.*, even and odd parity, the product is an odd function which has zero integral on the symmetric interval [–1,1].

II.1.4. Applications

II.1.4.1. High accuracy vibrational energy levels of H_2O up to near dissociation

Detailed knowledge of the spectroscopy of the water molecule is fundamental to a wide variety of scientific and engineering applications.[18] Due to its extreme importance, high-resolution spectra of the water isotopologues have been studied extensively.[19,20] Computational methods to study the rovibration states of water up to dissociation for a given potential energy surface (PES), although computationally demanding, have been available for more than a decade.[21,22,23] However, as also noted in Ref. 21, the available potential energy surfaces used in those earlier computations were not designed to be accurate in the high-energy regions approaching dissociation. Thus results obtained using these earlier PESs should be treated with caution.

Experimentally, higher-energy regions of the water potential started to be probed systematically by Rizzo et al. using two-[24,25] and three-photon[25,26,27,28] excitation schemes. These studies give insight into some of the vibrational states of H_2O all the way to dissociation, but they are sensitive only to states which are accessed by the excitation scheme applied. The ability to reach the vibrational levels all the way to dissociation represents a major advance; however, so far only a minority of the states could be observed. The lack of direct experimental measurement of higher vibrational states of water does not necessarily mean that such states are of no interest. For example, recent observations of cometary emission spectra suggest that highly excited vibrational states of water are naturally populated in comets,[29] although the mechanism for this is unknown.

In a recently published paper[30] a complete list of computed bound vibrational energy levels for water was presented almost all the way to dissociation obtained using a new, accurate, global, *ab initio* PES. Nuclear motion calculations were performed using several codes, including the D^2FOPI code I developed, in order to validate the computed results. Omitting the computational details and some other aspects of the article concerning quantum label assignment of the vibrational band origins (VBO), only a limited amount of the results are summarized here. The computations converged energy levels to better than 1 cm^{-1}, with the exception of an even symmetry state at about 40570 cm^{-1} which shows considerable sensitivity to the number of angular basis functions used. Energy levels computed with the different codes agreed to better than 1 cm^{-1} for all the VBOs reported. Altogether 1150 VBOs are supported by the PES chosen, with the highest one being at 41083 cm^{-1}. The last bound state assigned by the computations of even symmetry is at 41082.75 cm^{-1}, it is (19 0 0) in

normal-mode notation. The last assigned bound state of odd symmetry, (18 0 1), is at 41082.78 cm^{-1}. The results presented above show that the D^2FOPI protocol which is realized in a well developed and optimized code is an effective tool for scientific applications.

II.1.4.2. High accuracy rovibrational energy levels of H_3^+ and its isotopologues H_2D^+ and D_2H^+

H_3^+ has always been a benchmark system for high-level electronic-structure computations, see, for example Refs. 31, 32 and 33. Naturally, H_3^+ has also been a test case for polyatomic nuclear-motion computations starting with the work of Carney and Porter.[34] The importance of *ab initio* computations can be appreciated by the fact that the first laboratory observation of the H_3^+ infrared spectrum[35] and the first astronomical detection of H_3^+ in the ionosphere of Jupiter[36] both relied on theoretical predictions. Despite the simplicity of H_3^+, its (ro)vibrational spectrum in the visible region provided a considerable challenge for theory. Once the barrier to linearity at 10000 cm^{-1} is exceeded on the ground-state PES, the vibrations become floppy and sample vast regions of the PES. Experiments were limited, since as they advanced beyond this barrier, they struggled with the strong decrease of all spectral intensities by about a factor of a million compared to the fundamental transition,[37] while former first-principles predictions became increasingly inaccurate and lost their ability to guide experimental line searches and spectral identifications.[38]

Recent advances[39,40] in experiment and theory led to a remarkable breakthrough in the spectroscopy of H_3^+ and its isotopologues through an international collaboration I participated in. Experimentally, advances in the sensitivity of ion trap spectroscopy on H_3^+ were achieved allowing for the measurement of the frequencies of (ro)vibrational transitions extending far into the visible spectral range. Theoretically, calibration-quality *ab initio* adiabatic PESs have been determined for all isotopologues of the molecular ion H_3^+. The Born-Oppenheimer electronic structure computations used optimized explicitly correlated shifted Gaussian functions, and diagonal Born-Oppenheimer corrections (DBOC) were computed from the accurate electronic wave functions. Nuclear-motion computations utilizing this PES were carried out up to the energy region of 16000 cm^{-1} using several codes, including a modified version of D^2FOPI which makes explicit allowance for the inclusion of non-adiabatic effects by using different rotational and vibrational masses, as proposed in Ref. 41. This simple model results in an additional term in the Hamiltonian operator, which, however, does not change the structure of the Hamiltonian matrix when using the D^2FOPI protocol. Therefore the implementaion I had to perform becomes rather straightforward.

Vibrational energy computations for the H_3^+ molecule agree within the different codes to better than 0.01 cm^{-1} and reproduce experimental transitions with a standard deviation of about 0.1 cm^{-1}. The rovibrational transition frequencies for H_3^+, H_2D^+ and D_2H^+, when compared with high resolution measurements, reproduce all the known rovibrational levels of the H_3^+ isotopologues considered to better than 0.2 cm^{-1}. This represents an order-of-magnitude improvement compared to previous studies of transitions in the visible.

Tables 1 and 2 show some selected rovibrational energy levels obtained from D^2FOPI calculations and their comparison to experimental energy levels obtained with the *Maesured Active Rotational-Vibrational Energy Levels* (MARVEL) procedure[42] for H_2D^+ and D_2H^+, respectively. Choosing the MARVEL energy levels for comparison was motivated by the fact that the active database approach of MARVEL provides the most relaible experimental values up to date, provided there is a sufficient number of experimental data available. Computations presented in Tables 1 and 2 were carried out employing a vibrational basis set of (25,25,25), whereby (n_1,n_2,n_p) means n_1 and n_2 PO spherical-DVR functions (with 200 primitive spherical functions) for the two distance-type and n_p Legendre basis functions for the angle-type coordinates. Naturally, a complete set of $2J + 1$ rotational basis function were used in all cases. Following the notation of Ref. 5, the spherical oscillator basis functions of the R_1 and R_2 coordinates had parameters $R_1^{max} = 5.5$ bohr and $R_2^{max} = 5.5$ bohr, respectively. For the inclusion of the nonadiabatic effects in the simple model of Ref. 41, vibrational masses were chosen to be Moss masses,[43,44] *i.e.* $m_{D,vib}$=2.013810 u and $m_{H,vib}$=1.007537 u, while for rotational masses the nuclear masses $m_{D,rot}$=2.013550 u and $m_{H,rot}$=1.007276 u were used.

As one might observe in Tables 1 and 2, experimental and computed energy levels agree very well for both molecules. The theoretical error with respect to experiment seems to be generally larger for H_2D^+, which is probably originating from the model used to take non-adiabatic effects into account. It is noted, that in the case of D_2H^+, some of the MARVEL energies determined appear to be incorrect and were omitted. This is discussed in more detail in section Sec. II.2.5..

Table 1. Selected rovibrational energy levels of H_2D^+ obtained from D^2FOPI calculations (E^{D2FOPI}) and from experiment with the MARVEL procedure (E^{MARVEL}), all given in cm^{-1}. Differences (ΔE) between the two sets of energies along with rotational quantum numbers (J) are also given.

E^{MARVEL}	E^{D2FOPI}	ΔE	J	E^{MARVEL}	E^{D2FOPI}	ΔE	J	E^{MARVEL}	E^{D2FOPI}	ΔE	J
45.70	45.70	0.00	1	2568.48	2568.34	0.14	2	4343.47	4343.43	0.04	1
60.03	60.03	0.01	1	2569.57	2569.45	0.13	2	4361.67	4361.63	0.04	1
72.46	72.46	0.00	1	2580.28	2580.29	-0.01	3	4412.39	4412.34	0.05	2
131.65	131.64	0.02	2	2610.73	2610.59	0.14	3	4466.79	4466.75	0.04	2
138.86	138.84	0.02	2	2618.59	2618.45	0.14	3	4512.57	4512.43	0.13	1
175.94	175.94	0.00	2	2651.46	2651.46	0.00	3	4555.91	4555.74	0.17	2
218.65	218.66	-0.01	2	2664.26	2664.14	0.12	3	4677.27	4677.09	0.17	1
223.86	223.87	-0.01	2	2710.27	2710.15	0.12	3	6287.67	6287.62	0.05	0
251.41	251.38	0.04	3	2717.33	2717.21	0.12	3	6330.97	6330.92	0.05	1
254.07	254.02	0.05	3	2820.80	2820.69	0.11	3	6342.85	6342.79	0.05	1
326.17	326.16	0.01	3	2820.82	2820.71	0.11	3	6363.82	6363.77	0.05	1
354.78	354.78	0.00	3	2992.51	2992.49	0.01	0	6400.72	6400.56	0.16	0
376.34	376.36	-0.01	3	3038.18	3038.16	0.02	1	6441.92	6441.75	0.17	1
458.35	458.36	-0.02	3	3050.50	3050.48	0.02	1	6466.53	6466.38	0.15	1
459.83	459.85	-0.02	3	3063.31	3063.30	0.01	1	6479.44	6479.29	0.16	1
2205.88	2205.87	0.00	0	3123.32	3123.29	0.03	2	6519.07	6518.90	0.17	2
2246.70	2246.68	0.01	1	3128.88	3128.85	0.03	2	6537.05	6536.90	0.15	2
2258.80	2258.78	0.02	1	3167.13	3167.11	0.01	2	6622.44	6622.25	0.19	3
2278.43	2278.42	0.00	1	3203.84	3203.84	0.01	2	6646.29	6646.15	0.15	2
2318.37	2318.33	0.04	2	3209.82	3209.81	0.00	2	6649.45	6649.30	0.15	2
2322.75	2322.70	0.05	2	3241.30	3241.25	0.05	3	6991.58	6991.57	0.00	0
2335.44	2335.30	0.14	0	3243.00	3243.02	-0.02	3	7039.36	7039.36	0.01	1
2379.38	2379.37	0.01	2	3317.07	3317.05	0.02	3	7046.71	7046.70	0.01	1
2383.97	2383.83	0.14	1	3339.86	3339.84	0.01	3	7064.84	7064.83	0.00	1
2402.79	2402.66	0.14	1	3363.90	3363.90	0.00	3	7123.23	7123.21	0.02	2
2409.32	2409.18	0.13	1	3434.90	3434.90	0.00	3	7126.87	7126.85	0.02	2
2415.46	2415.42	0.04	3	3436.84	3436.85	-0.01	3	7177.98	7177.97	0.01	2

Table 2. Selected rovibrational energy levels of D_2H^+ obtained from D^2FOPI calculations (E^{D2FOPI}) and from experiment with the MARVEL procedure (E^{MARVEL}), all given in cm^{-1}. Differences (ΔE) between the two sets of energies along with rotational quantum numbers (J) are also given.

E^{MARVEL}	E^{D2FOPI}	ΔE	J	E^{MARVEL}	E^{D2FOPI}	ΔE	J	E^{MARVEL}	E^{D2FOPI}	ΔE	J
34.92	34.92	0.00	1	2136.24	2136.21	-0.03	1	2930.82	2930.78	-0.04	3
49.25	49.26	0.00	1	2136.50	2136.44	-0.05	3	2934.55	2934.51	-0.04	3
57.99	57.99	0.00	1	2145.62	2145.58	-0.04	2	2985.09	2985.06	-0.03	3
101.72	101.72	0.00	2	2149.56	2149.52	-0.04	2	3015.81	3015.78	-0.03	3
110.26	110.26	0.00	2	2194.06	2194.03	-0.04	2	3028.50	3028.48	-0.02	3
136.36	136.37	0.00	2	2202.78	2202.74	-0.04	2	3106.59	3106.57	-0.02	3
179.16	179.17	0.01	2	2205.80	2205.76	-0.04	3	3107.23	3107.22	-0.01	3
182.06	182.07	0.01	2	2225.16	2225.12	-0.03	2	3871.38	3871.30	-0.07	1
196.10	196.09	-0.01	3	2236.36	2236.32	-0.04	3	3881.70	3881.63	-0.07	1
200.03	200.02	-0.01	3	2253.05	2253.01	-0.04	3	3909.91	3909.84	-0.08	2
251.30	251.31	0.00	3	2254.67	2254.64	-0.03	2	3921.97	3921.89	-0.08	2
283.32	283.32	0.01	3	2257.58	2257.56	-0.03	2	4042.77	4042.71	-0.06	0
296.05	296.05	0.00	3	2297.58	2297.54	-0.04	3	4058.48	4058.42	-0.06	1
377.72	377.76	0.03	3	2306.74	2306.70	-0.04	3	4060.79	4060.75	-0.05	0
1968.16	1968.12	-0.05	0	2339.73	2339.71	-0.03	3	4062.89	4062.83	-0.06	1
1998.54	1998.49	-0.05	1	2350.97	2350.94	-0.03	3	4097.09	4097.00	-0.10	2
2014.11	2014.06	-0.05	1	2389.50	2389.47	-0.02	3	4097.90	4097.84	-0.07	2
2027.05	2027.01	-0.04	1	2397.50	2397.48	-0.02	3	4101.08	4101.01	-0.06	1
2055.10	2055.05	-0.05	2	2446.18	2446.18	-0.01	3	4119.11	4119.07	-0.04	1
2062.94	2062.89	-0.05	2	2771.51	2771.49	-0.03	1	4122.95	4122.90	-0.05	1
2078.43	2078.40	-0.04	0	2785.33	2785.30	-0.03	1	4130.79	4130.75	-0.05	1
2099.92	2099.88	-0.04	2	2793.95	2793.92	-0.03	1	4179.77	4179.72	-0.05	2
2118.59	2118.55	-0.04	1	2837.55	2837.52	-0.04	2	6482.03	6481.96	-0.08	1
2128.70	2128.66	-0.04	1	2845.72	2845.68	-0.04	2				
2133.50	2133.45	-0.05	3	2915.60	2915.58	-0.02	2				

II.1.5. Concluding remarks

As a short summary for this chapter, the theoretical background of the D^2FOPI algorithm for computing (ro)vibrational eigenpairs of triatomic molecules was presented along with demonstrating its efficiency through computation of nearly all the vibrational band origins of the H_2O molecule up to dissociation within cm^{-1} convergence and through the state of the art determination of rovibrational states of the H_3^+, H_2D^+ and D_2H^+ molecules with an accuracy to better than 0.2 cm^{-1} with respect to the available experimental values.

II.2. Assigning approximate quantum numbers

In the fourth age of quantum chemistry[45] codes implementing the variational solution of the time-independent nuclear-motion Schrödinger equation become more and more standard tools of theoretical molecular spectroscopy. Assigning exact and approximate quantum numbers to the large collection of computed eigenstates is important to turn data into knowledge, solve chemically significant problems, and develop self-consistent spectroscopic databases built upon spectroscopic networks.[42,46] Therefore, during the developing of a program suite on nuclear-motion computations, it is very useful to implement a protocol assigning approximate quantum numbers to the molecular states. To the best of my knowledge, assigning rovibrational quantum numbers in a theoretically rigorous manner can only be achieved by the rigid rotor decomposition (RRD) scheme of Ref. 47.

II.2.1. Theoretical background of the rigid rotor decomposition (RRD) scheme

The following description of the RRD scheme follows closely that given in Ref. 47.

For a closed-shell molecule, in the absence of an external field and when neglecting hyperfine interactions, the J rotational quantum number is a good quantum number for the description of the overall molecular rotation; thus, the labeling of the nuclear motion states can be done independently for different J values. Let us assume that the following three criteria are satisfied for an asymmetric-top molecule under investigation. (1) Given a J rotational quantum number, the rovibrational time-independent Schrödinger equation $\hat{H}^{\mathrm{rovib}}\Psi_n^{\mathrm{rovib}} = E_n^{\mathrm{rovib}}\Psi_n^{\mathrm{rovib}}, n \in \{1,2,\ldots,n_{\mathrm{rovib}}\}$ is solved for n_{rovib} number of eigenpairs. Furthermore, the rovibrational E_n^{rovib} energy levels and Ψ_n^{rovib} wave functions (functions of the rotational coordinates and the vibrational internal coordinates) are both available, but lack rovibrational quantum labels. (2) For the given J rotational quantum number, the rigid-rotor Schrödinger equation $\hat{H}^{\mathrm{RR}}\Phi_n^{\mathrm{RR}} = E_n^{\mathrm{RR}}\Phi_n^{\mathrm{RR}}$, $n \in \{1,2,\ldots,2J+1\}$ is also solved, providing $2J+1$ rotational wave functions for each vibrational state (for each vibrational state, a different set of effective rotational constants could be used). These wave functions depend on the rotational coordinates, and each of them can be characterized by a unique set of rotational quantum labels. In the case of asymmetric tops, these quantum numbers are $\{J, K_a, K_c\}$, where J is the quantum number corresponding to the overall rotational motion of the molecule, while K_a and K_c correspond to the projections of the rotational angular momentum

on the body-fixed z axis for the prolate and oblate symmetric-top limits of the rigid rotor, respectively. (3) The $J = 0$ pure vibrational Schrödinger equation $\hat{H}^{\text{vib}}\psi_n^{\text{vib}} = E_n^{\text{vib}}\psi_n^{\text{vib}}$, $n \in \{1,2,...,n_{\text{vib}}\}$ is solved for n_{vib} eigenpairs. A unique vibrational label is assigned to each vibrational eigenstate, which might be obtained for low-energy states using the normal mode decomposition (NMD) protocol described in Ref. 47.

The RRD scheme is based on a $(2J+1)\cdot n_{\text{vib}}$-dimensional $\left|\psi_k^{\text{vib}}\Phi_l^{\text{RR}}\right\rangle = \left|\psi_k^{\text{vib}}\right\rangle \otimes \left|\Phi_l^{\text{RR}}\right\rangle$, $k \in \{1,2,...,n_{\text{vib}}\}, l \in \{1,2,...,2J+1\}$, orthonormal, direct-product basis. Therefore, each direct-product basis function has a unique rovibrational label.

The next step is the computation of the overlaps

$$S_{n;k,l} = \left\langle \Psi_n^{\text{rovib}} \middle| \psi_k^{\text{vib}}\Phi_l^{\text{RR}} \right\rangle, n \in \{1,2,...,n_{\text{rovib}}\}, k \in \{1,2,...,n_{\text{vib}}\}, l \in \{1,2,...,2J+1\}. \quad (11)$$

Then, for each Ψ_n^{rovib} the quantities $P_{n;k} = \sum_{l=1}^{2J+1} S_{n;k,l}^2$ are evaluated. These quantities are interpreted as the "total overlap" of the kth vibrational state and the nth rovibrational state. For each value of n, $k_n^{\max}$ is determined, $P_{n;k_n^{\max}}$ being the largest of the $P_{n;k}$ values. Finally, Ψ_n^{rovib} is labeled with the rovibrational quantum numbers of the direct-product basis function with which its $S_{n;k_n^{\max},l}$ overlap is the largest. Naturally, to obtain unique labels $(2J+1)\cdot n_{\text{vib}} \geq n_{\text{rovib}}$ must hold.

II.2.2. The RRD package for D^{2}FOPI

An RRD program was developed in order to execute an RRD analysis based on D^{2}FOPI computations. As input, the RRD code needs the D^{2}FOPI vibrational and rovibrational energies along with the wave functions represented in the basis of the D^{2}FOPI computation. Vibrational quantum labels are also needed as input. Beyond the D^{2}FOPI (ro)vibrational output files, the RRD package naturally requires rigid-rotor (RR) wavefunctions with corresponding labels. The computation of the rigid-rotor eigenpairs is performed by representing the rigid-rotor Hamiltonian on the same $C_{MK}^{Jp}(\varphi,\chi,\psi)$, $p \in \{0,1\}, K \in \{p, p+1,...,J-1,J\}$ rotational basis which is used for the rovibrational D^{2}FOPI calculations in order to make the $S_{n;k,l} = \left\langle \Psi_n^{\text{rovib}} \middle| \psi_k^{\text{vib}}\Phi_l^{\text{RR}} \right\rangle$ RRD overlap computations straightforward. The RR Hamiltonian reads as

$$\hat{H}^{\text{RR}} = A\hat{J}_x^2 + B\hat{J}_y^2 + C\hat{J}_z^2 = \alpha\hat{J}^2 + \beta\hat{J}_z^2 + \gamma\left(\hat{J}_+^2 + \hat{J}_-^2\right), \quad (12)$$

where A, B, and C are rotational constants for the given vibrational state, $\hat{J}_i$ is the ith component of the total angular momentum operator, $\hat{J}^2 = \hat{J}_x^2 + \hat{J}_y^2 + \hat{J}_z^2$, $\alpha = \frac{1}{2}(A+B)$, $\beta = C - \frac{1}{2}(A+B)$, $\gamma = \frac{1}{4}(A-B)$, and $\hat{J}_\pm = \hat{J}_x \pm i\hat{J}_y$. In the basis of the $C_{MK}^{Jp}(\varphi,\chi,\psi)$ symmetry-adapted rotational basis functions, the $(2J+1)\times(2J+1)$-dimensional $\mathbf{H}_{\text{rot}}$ matrix is block diagonal having a J- and a $(J+1)$-dimensional block for $p = 1$ and $p = 0$, respectively. An element of the Hamiltonian can be written as

$$\left(\mathbf{H}_{\text{rot}}\right)_{pK,p'K'} = \delta_{p,p'}\alpha\left(\mathbf{J}^2\right)_{K,K'} + \delta_{p,p'}\beta\left(\mathbf{J}_z^2\right)_{K,K'} + \delta_{p,p'}\gamma\left(\mathbf{J}_+^2 + \mathbf{J}_-^2\right)_{K,K'} \tag{13}$$

where

$\left(\mathbf{J}^2\right)_{K,K'} = \delta_{K,K'}J(J+1)$, $\left(\mathbf{J}_z^2\right)_{K,K'} = \delta_{K,K'}K^2$, and

$$\left(\mathbf{J}_+^2 + \mathbf{J}_-^2\right)_{K,K'} = \delta_{K,K'+2}\sqrt{1+\delta_{K,2}\delta_{K',0}}\sqrt{J(J+1)-K'(K'+1)}\sqrt{J(J+1)-(K'+1)(K'+2)} +$$
$$\delta_{K,K'-2}\sqrt{1+\delta_{K,0}\delta_{K',2}}\sqrt{J(J+1)-K'(K'-1)}\sqrt{J(J+1)-(-K'+1)(-K'+2)} + \delta_{K,1}\delta_{K',1}(-1)^p J(J+1)$$

with $K \in \{p, p+1, \ldots, J-1, J\}$.

II.2.3. Embedding dependence of the RRD

RRD overlaps $S_{n;k_n^{\max},J}$ depend on the embedding of the molecule-fixed axis system chosen. Investigation of this dependence is the topic of the present section.

RRD overlaps for the H_2O molecule, chosen as our test system, are determined using Jacobi coordinates with either the R_1 or bisector embeddings,[4] and employing the D^{2}FOPI protocol. Although in the case of the bisector embedding the use of Radau coordinates might seem to be a better choice for computing RRD overlaps, test computations showed that RRD coefficients obtained with Radau coordinates are essentially identical with the ones obtained using Jacobi coordinates. Computations were also performed with valence internal coordinates and an Eckart embedding.[48] In the bisector embedding, the x-axis of the body-fixed frame is chosen to bisect the angle between the interatomic vector of the diatom (O-H) and the vector connecting the center of mass of the diatom with the third atom (H). In the Eckart embedding, the body-fixed frame is chosen such that the nuclei satisfy the Eckart conditions.[48]

In order to make the body-fixed embeddings closer to the principal-axis system, in which the rigid-rotor computations were carried out, unorthodox choices were made for the R_1 and bisector embeddings during the present study. Within the R_1 embedding the molecule was

placed in the (z,x)-plane with the body-fixed z-axis chosen to lie along the two H atoms, the x-axis "looking towards" the O atom in the plane of the molecule, and the y-axis chosen to give a right-handed coordinate system. In the bisector embedding the molecule was placed in the (z,x)-plane with the body fixed x-axis chosen to bisect the HOH bond angle in symmetric configurations.

In the case of the Eckart embedding, the computations were based on the transformation method proposed in Ref. 49 and utilizing a different code, *i.e.*, using the GENIUSH (*GEneral code with Numerical, Internal coordinate, User-Specified Hamiltonians*) program suite which uses a fully numerical grid representation of the Hamiltonian. Interested readers should consult Refs. 50 and 51 for details on the GENIUSH protocol. Although the explicit form of the Hamiltonian in the Eckart embedding with Jacobi coordinates has been derived for the triatomic case,[52] the fully numerical GENIUSH approach was chosen for the sake of minimal programming work.

II.2.3.1. Computational details

As written earlier, the test system chosen for the investigations on the embedding dependence of the RRD is the $H_2{}^{16}O$ isotopologue of the water molecule. The PES of Ref. 53 was employed in all nuclear motion computations. This choice makes comparison of the present results with those of the BT2 linelist[54] straightforward. Masses m_O=15.9994 u and m_H=1.00794 u were used throughout the RRD analysis.

For both the determination of the $J = 0$ (vibrational) and $J \neq 0$ (rovibrational) eigenpairs in the R_1 and bisector embeddings, the D^{2}FOPI program suite[5] was used. For the rigid-rotor computations the rotational constants were chosen, in cm^{-1}, as A = 14.5964, B = 9.5274, and C = 27.4348 when using the R_1 embedding, while A = 9.5274, B = 14.5964, and C = 27.4348 when using the bisector embedding. The same rotational constants are employed for all vibrational states. It appears to be natural to compute RRD overlaps using the vibrationally-averaged rotational constants of each vibrational state. Our computations in the R_1 embedding for the J = 15 case showed, however, that even a major change in the rotational constants, *i.e.*, employing A = 15.2770, B = 8.4600, and C = 73.0396 which correspond to the (0 5 0) excited bending state, resulted in no change in the list of RRD labels which could be used for assignation (later introduced as "well-defined" RRD labels).

When using the R_1 or bisector embeddings, the variational (ro)vibrational computations on the H_2O molecule were performed using (15,20,30) and (20,25,35) vibrational basis

functions, respectively, whereby (n_1,n_2,n_p) means n_1 and n_2 PO spherical-DVR functions (with 300 primitive spherical functions) for the two distance-type and n_p Legendre basis functions for the angle-type coordinates. Naturally, a complete set of $2J+1$ rotational basis functions was used in all cases. Following the notation of Ref. 5, the spherical oscillator basis functions of the R_1 and R_2 coordinates had parameters R_1^{max} = 4.6 bohr and R_2^{max} = 3.2 bohr, respectively.

When using the Eckart embedding via the GENIUSH algorithm, valence coordinates (OH bond lengths r_1 and r_2, HOH bond angle Θ) were employed. The applied direct-product vibrational basis consisted of 20 PO Hermite-DVR functions (with 80 primitive Hermite polynomials) for the two stretching coordinates and 30 Legendre-DVR functions for the bending coordinate. The GENIUSH computations utilized Wang combinations of the well-known symmetric top eigenfunctions as rotational basis functions.

II.2.3.2. Embedding, energy, and J dependence of the RRD scheme

Following the RRD scheme, rovibrational quantum labels were generated for the H_2O molecule for all three embeddings and for rotational quantum numbers J = 5, 10 and 15 for 30×(2J+1) rovibrational eigenstates for each J. Vibrational normal-mode labels (n_1 n_2 n_3) were taken from Ref. 30 by matching energies, which is straightforward for the vibrational states considered, while the rotational asymmetric top limit $J_{K_aK_c}$ labels were generated during the rigid-rotor computations following the standard rigid-rotor labeling scheme.[11]

In terms of rovibrational states being the linear combination of the direct-product functions obtained from vibrational and rigid-rotor eigenfunctions, rovibrational states become more "mixed" with increasing energy and J rotational quantum number. This naturally leads to less dominant RRD overlaps (see Eq. (11)). Figs. 2, 3 and 4 show the percentage of clearly assignable rovibrational states as a function of rovibrational energy for J = 5, 10, and 15, respectively. Each figure includes results for three embeddings. RRD labels were considered "well defined" if for the given rovibrational state the square of the largest $S_{n;k_n^{max},J}$ coefficient from Eq. (11) exceeded 0.5, as implied by the Hose–Taylor theorem.[55] As expected, less and less RRD labels are "well defined" with increasing J quantum number and energy. Nonetheless, for a wide range of both of these parameters a large number of "well defined" labels can be assigned via the RRD protocol. Out of the total

of 1865 states included in Figs. 2, 3 and 4, 973, 1211 and 1288 states could be given a "well defined" status when using the R_1, bisector, and Eckart embeddings, respectively.

It is to be noted that the choice of 0.5 as a lower limit for the square of the largest $S_{n;k_n^{\max},J}$ coefficients for considering an RRD label "well defined" is not the only one possible. With a lower threshold, one could extend the range of applicability of the RRD scheme considerably; however, this might lead to embedding-dependent quantum labels and in a few cases to duplicate labels. For example, choosing a cut-off value of 0.33, one obtains 1368, 1566, and 1596 well-defined labels for the R_1, bisector, and Eckart embeddings, respectively, but out of these 10, 17, and 25 are assigned twice and in 21 cases the assigned RRD labels are embedding dependent, *i.e.*, the assigned labels differ in the different embeddings.

Another strategy is to consider an RRD label well defined if the second largest $S_{n;k_n^{\max},J}$ overlap is smaller than some portion of the largest $S_{n;k_n^{\max},J}$ overlap. Although with this method the number of well-defined labels can be dramatically increased, it leads, unfortunately, to some duplicate labels. Curing this problem needs special attention and the procedure cannot be automated.

As seen clearly in Figs. 2, 3 and 4, the RRD coefficients depend noticeably on the embedding used for the rovibrational computations. Naturally, one expects and indeed experiences the least RRD "mixing" when the coupling between the rotational and vibrational coordinates is minimal, *i.e.*, in the Eckart embedding. The Eckart embedding is clearly the best choice especially at the lower end of the spectrum. Although the Eckart embedding minimizes the coupling between molecular rotations and vibrations, Fig. 4 shows the "breakdown" of the Eckart embedding farther away from the equilibrium structure. At higher rotational excitation and energies rovibrational coupling is considerable even in the Eckart embedding, which is represented by the small maximum RRD coefficient values in such spectral regions. For the computation of rovibrational eigenstates an embedding different from the Eckart one might be more efficient. In a given application, one has to find a balance between computational efficiency and "mixing" of the RRD coefficients and choose the embedding accordingly.

Finally, the relation between monodromy[56-59] and RRD label assignment is examined. Quantum monodromy,[60] which leads to a change in the energy level structure when a bent molecule starts to sample linear configurations, was discussed for the $H_2{}^{16}O$ water isotopologue in Ref. 61. As noted by Zobov et al.,[61] "*monodromy in quantum mechanical*

systems implies the absence of a single, smoothly varying set of quantum numbers with which to characterize the system." Monodromy might explain the breakdown of the RRD protocol when high excitation of the bending mode is involved. Rovibrational states for the H_2O molecule with vibrational labels, which include excitations for only a single normal mode, were included in Fig. 5 to compare the energy dependence of the $S_{n;k_n^{\max},J}$ overlap values for rovibrational states with different types of vibrational excitation. Inspecting the red squares in Fig. 5, standing for rovibrational states with the largest $S_{n;k_n^{\max},J}$ overlap within a given vibrational state, one can observe that states having pure bending excitations (plots with $(0\,n\,0)$) show a breakdown in the $S_{n;k_n^{\max},J}$ overlap values from around 10000 cm^{-1}, close to the barrier to linearity of water.[62-64] Thus, it seems that monodromy might at least partially explain the breakdown of the RRD method for rovibrational states with high bending excitation. Such a breakdown is not observable for the symmetric $(n\,0\,0)$ and antisymmetric $(0\,0\,n)$ stretching states. Nevertheless, as the n and J values increase the stretching states also start exhibiting smaller and smaller maximum RRD coefficients.

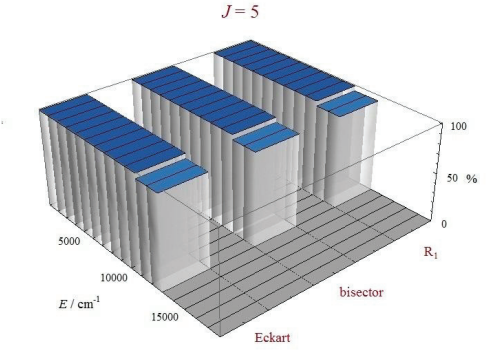

Figure 2. Percentage of clearly assignable rovibrational states during the RRD analysis as a function of rovibrational energy in the R_1, bisector, and Eckart embeddings, for $J = 5$ rotational excitation.

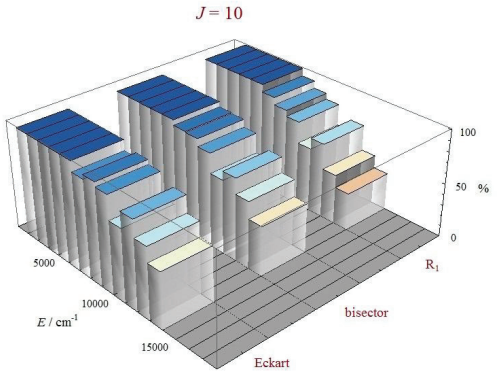

Figure 3. Percentage of clearly assignable rovibrational states during the RRD analysis as a function of rovibrational energy in the R_1, bisector, and Eckart embeddings, for $J = 10$ rotational excitation.

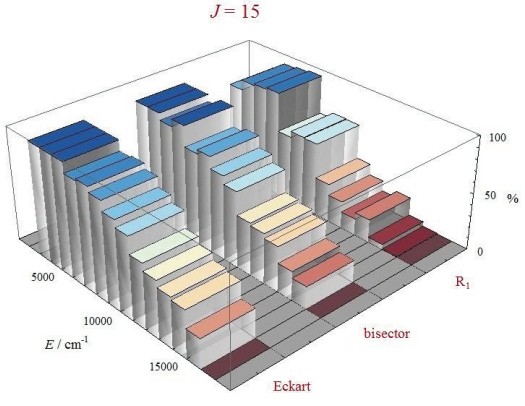

Figure 4. Percentage of clearly assignable rovibrational states during the RRD analysis as a function of rovibrational energy in the R_1, bisector, and Eckart embeddings, for $J = 15$ rotational excitation.

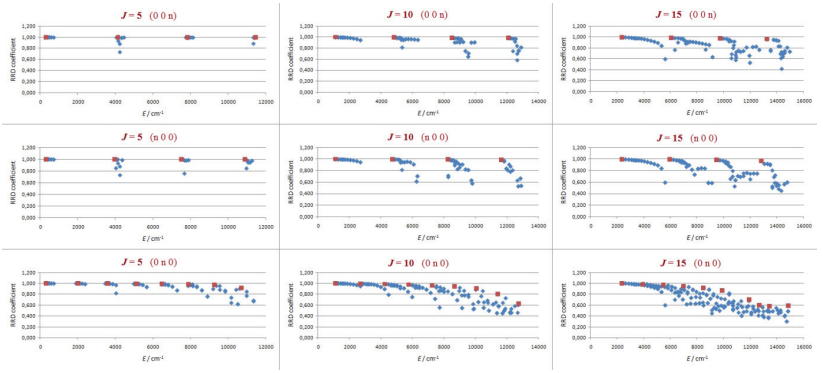

Figure 5. The largest RRD coefficients obtained in the Eckart embedding as a function of rovibrational energy. (n 0 0), (0 0 n), and (0 n 0) refer to approximate vibrational quantum labels for symmetric stretch, antisymmetric stretch, and bend, respectively. In all these cases the states included in the given plot have vibrational quantum labels such that all normal modes but the one excited by n quanta are in their ground state. Blue rectangles stand for rovibrational states while red squares depict rovibrational states with the largest RRD overlap within a given vibrational manifold.

II.2.4. Validation of quantum labels for H_2O, comparison with the BT2 linelist

One of the linelists available for $H_2{}^{16}O$ is the so-called BT2 linelist.[54] When comparing the "well defined" rovibrational labels of $H_2{}^{16}O$ obtained using the RRD in the Eckart embedding, with the labels found in the BT2 linelist, one can observe and appreciate the usefulness of the RRD labeling protocol.

Based on this comparison, one might divide the calculated rovibrational states into five groups: (a) states which are assigned both in the BT2 and during the RRD but have different labels in the two cases, (b) rovibrational states which are assigned both in the BT2 linelist and during the RRD and have the same labels in the two cases, (c) states which have an assigned label in the BT2 linelist but are not assigned during the RRD, (d) states which are assigned during the RRD but have no assignment in the BT2, and finally (e) states which are not assigned in either the BT2 or during the RRD. In Fig. 6 rovibrational states of H_2O are separated according to their (a)-(e) type and are marked on the figure based on their energy.

As expected, for lower-energy states both the RRD scheme and the protocol employed when generating the BT2 linelist provide assigned labels which are in great agreement. It is only at around 5500 cm^{-1} that a few states start to show "mixing" in the RRD and thus cease to be "well defined".

The few dozen cases where both BT2 and RRD have assigned but different labels need special attention and need to be ispected individually. The RRD scheme is thus useful not only to provide labels for yet unassigned states but also to validate existing labels.

The usefulness of the RRD scheme can especially be appreciated from about 10000 cm^{-1}, where the BT2 linelist starts lacking assigned labels. From around 10000 cm^{-1} up to around 15000 cm^{-1}, there are many states which don't have BT2 labels, but can be assigned one via the RRD scheme.

The number of states lacking RRD labels, as seen in Fig. 6, naturally increases with energy. One might notice that from around 10000 cm^{-1} states lacking any assignment start appearing quite suddenly. The explanation of this behavior may again involve arguments based on quantum monodromy.[61]

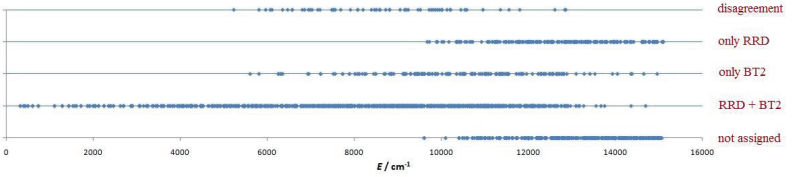

Figure 6. $J = 5$, $J = 10$, and $J = 15$ rovibrational states of H_2O separated according to their (a)-(e) type (see Sec. VI) and marked on the figure based on their energy.

II.2.5. Validation of quantum labels for H_2D^+ and D_2H^+

As detailed on the example of the BT2 linelist in the previous section, the rigorous approximate quantum label assignation scheme of the RRD protocol provides a powerful tool for validating existing quantum labels of molecules. This validation is rather important, for example, when one deduces experimental energy levels from measured transitions using the MARVEL procedure, since the method relies strongly on selection rules realized by the allowable changes in rovibrational quantum numbers. For this reason, the RRD analysis based on D^2FOPI computations was used to validate previously assigned quantum labels for H_2D^+

and D_2H^+. The basis sets and PES used for the (ro)vibrational computations were identical to the ones detailed in Sec. I.4.2., while for the computation of the rigid rotor eigenfunctions, the rotational constants A = 43.362, B = 16.610, C = 29.143 and A = 21.869, B = 13.057, C = 36.243, all in cm^{-1}, were used for H_2D^+ and D_2H^+, respectively. Out of the 75 experimentally available and assigned states considered for H_2D^+, 70 could be assigned a well defined RRD label which all agreed with the previous labels used by MARVEL. The situation is different for D_2H^+, where out of the 74 considered states 73 had a well defined RRD label, from which 5 cases were found to be problematic, *i.e.*, the MARVEL energies and D^2FOPI energies differ significantly.

Table 3 and 4 summarizes all the considered rovibrational states, their RRD overlaps, rovibrational symmetry, and finally the MARVEL and RRD assigned quantum labels for H_2D^+ and D_2H^+, respectively. In Table 3 the experimental energy levels and quantum labels show outstanding agreement with their *ab initio* counterparts, H_2D^+ seems to be precisely characterized and validated for the states considered. As for D_2H^+, the situation is similar for the majority of the considered states; however, the 5 states having D^2FOPI energies of 2871.44 cm^{-1}, 2912.67 cm^{-1}, 6465.95 cm^{-1}, 6538.40 cm^{-1} and 6567.70 cm^{-1}, differ from MARVEL counterparts by 0.19 cm^{-1}, 0.57 cm^{-1}, 58.97 cm^{-1}, 32.47 cm^{-1} and 166.71 cm^{-1}, respectively. They need special attention due to the fact that the average absolute energy difference when excluding these 5 states is 0.03 cm^{-1} with a standard deviation of 0.02 cm^{-1}. Since all the D^2FOPI results are based on the same *ab initio* protocol, they should have about the same error in such small spectral region. Therefore the outliers probably originate from missassignments of some transitions in the original sources employed in the MARVEL procedure.

Table 3. Rovibrational energies, vibrational normal mode ($n_1n_2n_3$) and rotational asymmetric top (J_{KaKc}) quantum labels, rovibrational symmetry (Symm) and largest RRD coefficients (RRD) for selected rovibrational states of H_2D^+, obtained with the MARVEL or the D^2FOPI based RRD algorithms. Energies are given in cm^{-1}, with respect to the zero point vibrational energy, symmetry labels refer to the irreducible representations of the C_{2v}(M) molecular symmetry group.[65]

MARVEL			D2FOPI					MARVEL			D2FOPI				
Energy	$(n_1n_2n_3)$	J_{KaKc}	Energy	$(n_1n_2n_3)$	J_{KaKc}	Symm	RRD	Energy	$(n_1n_2n_3)$	J_{KaKc}	Energy	$(n_1n_2n_3)$	J_{KaKc}	Symm	RRD
45.70	0 0 0	1_{01}	45.70	0 0 0	1_{01}	B1	0.995	3063.31	1 0 0	1_{10}	3063.30	1 0 0	1_{10}	B2	1.000
60.03	0 0 0	1_{11}	60.03	0 0 0	1_{11}	A2	0.995	3123.32	1 0 0	2_{02}	3123.29	1 0 0	2_{02}	A1	0.978
72.46	0 0 0	1_{10}	72.46	0 0 0	1_{10}	B2	1.000	3128.88	1 0 0	2_{12}	3128.85	1 0 0	2_{12}	B2	0.977
131.65	0 0 0	2_{02}	131.64	0 0 0	2_{02}	A1	0.980	3167.13	1 0 0	2_{11}	3167.11	1 0 0	2_{11}	A2	0.993
138.86	0 0 0	2_{12}	138.84	0 0 0	2_{12}	B2	0.979	3203.84	1 0 0	2_{21}	3203.84	1 0 0	2_{21}	B1	0.995
175.94	0 0 0	2_{11}	175.94	0 0 0	2_{11}	A2	0.994	3209.82	1 0 0	2_{20}	3209.81	1 0 0	2_{20}	A1	0.998
218.65	0 0 0	2_{21}	218.66	0 0 0	2_{21}	B1	0.995	3241.30	1 0 0	3_{03}	3241.25	1 0 0	3_{03}	B1	0.742
223.86	0 0 0	2_{20}	223.87	0 0 0	2_{20}	A1	0.999	3243.00	1 0 0	3_{13}	3243.02	1 0 0	3_{13}	A2	0.950
251.41	0 0 0	3_{03}	251.38	0 0 0	3_{03}	B1	0.764	3317.07	1 0 0	3_{12}	3317.05	1 0 0	3_{12}	B2	0.783
254.07	0 0 0	3_{13}	254.02	0 0 0	3_{13}	A2	0.954	3339.86	1 0 0	3_{22}	3339.84	1 0 0	3_{22}	A1	0.977
326.17	0 0 0	3_{12}	326.16	0 0 0	3_{12}	B2	0.769	3363.90	1 0 0	3_{21}	3363.90	1 0 0	3_{21}	B1	0.765
354.78	0 0 0	3_{22}	354.78	0 0 0	3_{22}	A1	0.979	3434.90	1 0 0	3_{31}	3434.90	1 0 0	3_{31}	A2	0.994
376.34	0 0 0	3_{21}	376.36	0 0 0	3_{21}	B1	0.784	3436.84	1 0 0	3_{30}	3436.85	1 0 0	3_{30}	B2	0.806
458.35	0 0 0	3_{31}	458.36	0 0 0	3_{31}	A2	0.995	4343.47	0 2 0	1_{11}	4343.43	0 2 0	1_{11}	A2	0.975
459.83	0 0 0	3_{30}	459.85	0 0 0	3_{30}	B2	0.789	4361.67	0 2 0	1_{10}	4361.63	0 2 0	1_{10}	B2	1.000
2246.70	0 1 0	1_{01}	2246.68	0 1 0	1_{01}	B1	0.968	4412.39	0 2 0	2_{12}	4412.34	0 2 0	2_{12}	B2	0.892
2258.80	0 1 0	1_{11}	2258.78	0 1 0	1_{11}	A2	0.964	4466.79	0 2 0	2_{11}	4466.75	0 2 0	2_{11}	A2	0.968
2278.43	0 1 0	1_{10}	2278.42	0 1 0	1_{10}	B2	1.000	4512.57	0 1 1	1_{11}	4512.43	0 1 1	1_{11}	B1	0.904
2318.37	0 1 0	2_{02}	2318.33	0 1 0	2_{02}	A1	0.892	4555.91	0 1 1	2_{02}	4555.74	0 1 1	2_{02}	B2	0.746
2322.75	0 1 0	2_{12}	2322.70	0 1 0	2_{12}	B2	0.887	4677.27	0 0 2	1_{11}	4677.09	0 0 2	1_{11}	A2	0.929
2379.38	0 1 0	2_{11}	2379.37	0 1 0	2_{11}	A2	0.970	6330.97	0 3 0	1_{01}	6330.92	0 3 0	1_{01}	B1	0.948
2383.97	0 0 1	1_{01}	2383.83	0 0 1	1_{01}	A2	0.952	6342.85	0 3 0	1_{11}	6342.79	0 3 0	1_{11}	A2	0.958
2402.79	0 0 1	1_{11}	2402.66	0 0 1	1_{11}	B1	0.956	6363.82	0 3 0	1_{10}	6363.77	0 3 0	1_{10}	B2	1.000
2409.32	0 0 1	1_{10}	2409.18	0 0 1	1_{10}	A1	1.000	6441.92	0 2 1	1_{01}	6441.75	0 2 1	1_{01}	A2	0.920
2415.46	0 1 0	2_{21}	2415.42	0 1 0	3_{03}	B1	0.614	6466.53	0 2 1	1_{11}	6466.38	0 2 1	1_{11}	B1	0.913
2568.48	0 0 1	2_{21}	2568.34	0 0 1	2_{21}	A2	0.960	6479.44	0 2 1	1_{10}	6479.29	0 2 1	1_{10}	A1	1.000
2569.57	0 0 1	2_{20}	2569.45	0 0 1	2_{20}	B2	0.980	6519.07	0 2 1	2_{02}	6518.90	0 2 1	2_{02}	B2	0.725
2580.28	0 1 0	3_{21}	2580.29	0 1 0	3_{21}	B1	0.728	6537.05	0 2 1	2_{12}	6536.90	0 2 1	2_{12}	A1	0.664
2610.73	0 0 1	3_{03}	2610.59	0 0 1	3_{03}	A2	0.694	6622.44	0 2 1	3_{03}	6622.25	0 3 0	3_{13}	A2	0.535
2618.59	0 0 1	3_{13}	2618.45	0 0 1	3_{13}	B1	0.711	6646.29	0 2 1	2_{21}	6646.15	0 2 1	2_{21}	A2	0.909
2651.46	0 1 0	3_{31}	2651.46	0 1 0	3_{31}	A2	0.946	6649.45	0 2 1	2_{20}	6649.30	0 2 1	2_{20}	B2	0.965
2664.26	0 0 1	3_{12}	2664.14	0 0 1	3_{30}	A1	0.656	7039.36	1 2 0	1_{01}	7039.36	1 2 0	1_{01}	B1	0.978
2710.27	0 0 1	3_{22}	2710.15	0 0 1	3_{22}	B2	0.846	7046.71	1 2 0	1_{11}	7046.70	1 2 0	1_{11}	A2	0.982
2717.33	0 0 1	3_{21}	2717.21	0 0 1	3_{21}	A2	0.757	7064.84	1 2 0	1_{10}	7064.83	1 2 0	1_{10}	B2	1.000
2820.80	0 0 1	3_{30}	2820.69	0 0 1	3_{30}	A1	0.740	7123.23	1 2 0	2_{02}	7123.21	1 2 0	2_{02}	A1	0.906
2820.82	0 0 1	3_{31}	2820.71	0 0 1	3_{31}	B1	0.958	7126.87	1 2 0	2_{12}	7126.85	1 2 0	2_{12}	B2	0.896
3038.18	1 0 0	1_{01}	3038.16	1 0 0	1_{01}	B1	0.994	7177.98	1 2 0	2_{11}	7177.97	1 2 0	2_{11}	A2	0.970
3050.50	1 0 0	1_{11}	3050.48	1 0 0	1_{11}	A2	0.995								

Table 4. Rovibrational energies, vibrational normal mode ($n_1n_2n_3$) and rotational asymmetric top (J_{KaKc}) quantum labels, rovibrational symmetry (Symm) and largest RRD coefficients (RRD) for selected rovibrational states of D_2H^+, obtained with the MARVEL or the D^2FOPI based RRD algorithms. Energies are given in cm^{-1}, with respect to the zero point vibrational energy, symmetry labels refer to the irreducible representations of the C_{2v}(M) molecular symmetry group.[65] Problematic states are in bold.

MARVEL			D2FOPI					MARVEL			D2FOPI				
Energy	$(n_1n_2n_3)$	J_{KaKc}	Energy	$(n_1n_2n_3)$	J_{KaKc}	Symm	RRD	Energy	$(n_1n_2n_3)$	J_{KaKc}	Energy	$(n_1n_2n_3)$	J_{KaKc}	Symm	RRD
34,92	0 0 0	$1_{0\,1}$	34,92	0 0 0	$1_{0\,1}$	B1	0,998	2339,73	0 1 0	$3_{3\,1}$	2339,71	0 1 0	$3_{3\,1}$	A2	0,781
49,25	0 0 0	$1_{1\,1}$	49,26	0 0 0	$1_{1\,1}$	A2	0,998	2350,97	0 0 1	$3_{1\,2}$	2350,94	0 0 1	$3_{1\,2}$	A2	0,903
57,99	0 0 0	$1_{1\,0}$	57,99	0 0 0	$1_{1\,0}$	B2	1,000	2389,50	0 0 1	$3_{2\,2}$	2389,47	0 1 0	$3_{3\,0}$	B2	0,685
101,72	0 0 0	$2_{0\,2}$	101,72	0 0 0	$2_{0\,2}$	A1	0,993	2397,50	0 0 1	$3_{2\,1}$	2397,48	0 0 1	$3_{2\,1}$	A1	0,788
110,26	0 0 0	$2_{1\,2}$	110,26	0 0 0	$2_{1\,2}$	B2	0,992	2446,18	0 0 1	$3_{3\,1}$	2446,18	0 0 1	$3_{3\,1}$	B2	0,985
136,36	0 0 0	$2_{1\,1}$	136,37	0 0 0	$2_{1\,1}$	A2	0,998	2771,51	1 0 0	$1_{0\,1}$	2771,49	1 0 0	$1_{0\,1}$	B1	0,998
179,16	0 0 0	$2_{2\,1}$	179,17	0 0 0	$2_{2\,1}$	B1	0,998	2785,33	1 0 0	$1_{1\,1}$	2785,30	1 0 0	$1_{1\,1}$	A2	0,998
182,06	0 0 0	$2_{2\,0}$	182,07	0 0 0	$2_{2\,0}$	A1	0,999	2793,95	1 0 0	$1_{1\,0}$	2793,92	1 0 0	$1_{1\,0}$	B2	1,000
196,10	0 0 0	$3_{0\,3}$	196,09	0 0 0	$3_{0\,3}$	B1	0,984	2837,55	1 0 0	$2_{0\,2}$	2837,52	1 0 0	$2_{0\,2}$	A1	0,993
200,03	0 0 0	$3_{1\,3}$	200,02	0 0 0	$3_{1\,3}$	A2	0,982	2845,72	1 0 0	$2_{1\,2}$	2845,68	1 0 0	$2_{1\,2}$	B2	0,992
251,30	0 0 0	$3_{1\,2}$	251,31	0 0 0	$3_{1\,2}$	B2	0,994	**2871,25**	**1 0 0**	**$2_{1\,1}$**	**2871,44**	**1 0 0**	**$2_{1\,1}$**	**A2**	**0,998**
283,32	0 0 0	$3_{2\,2}$	283,32	0 0 0	$3_{2\,2}$	A1	0,992	**2912,10**	**1 0 0**	**$2_{2\,1}$**	**2912,67**	**1 0 0**	**$2_{2\,1}$**	**B1**	**0,997**
296,05	0 0 0	$3_{2\,1}$	296,05	0 0 0	$3_{2\,1}$	B1	0,997	2915,60	1 0 0	$2_{2\,0}$	2915,58	1 0 0	$2_{2\,0}$	A1	0,999
377,72	0 0 0	$3_{3\,0}$	377,76	0 0 0	$3_{3\,0}$	B2	0,996	2930,82	1 0 0	$3_{0\,3}$	2930,78	1 0 0	$3_{0\,3}$	B1	0,983
1998,54	0 1 0	$1_{0\,1}$	1998,49	0 1 0	$1_{0\,1}$	B1	0,985	2934,55	1 0 0	$3_{1\,3}$	2934,51	1 0 0	$3_{1\,3}$	A2	0,981
2014,11	0 1 0	$1_{1\,1}$	2014,06	0 1 0	$1_{1\,1}$	A2	0,973	2985,09	1 0 0	$3_{1\,2}$	2985,06	1 0 0	$3_{1\,2}$	B2	0,994
2027,05	0 1 0	$1_{1\,0}$	2027,01	0 1 0	$1_{1\,0}$	B2	1,000	3015,81	1 0 0	$3_{2\,2}$	3015,78	1 0 0	$3_{2\,2}$	A1	0,991
2055,10	0 1 0	$2_{0\,2}$	2055,05	0 1 0	$2_{0\,2}$	A1	0,947	3028,50	1 0 0	$3_{2\,1}$	3028,48	1 0 0	$3_{2\,1}$	B1	0,996
2062,94	0 1 0	$2_{1\,2}$	2062,89	0 1 0	$2_{1\,2}$	B2	0,929	3106,59	1 0 0	$3_{3\,1}$	3106,57	1 0 0	$3_{3\,1}$	A2	0,995
2099,92	0 1 0	$2_{1\,1}$	2099,88	0 1 0	$2_{1\,1}$	A2	0,990	3107,23	1 0 0	$3_{3\,0}$	3107,22	1 0 0	$3_{3\,0}$	B2	0,995
2118,59	0 0 1	$1_{0\,1}$	2118,55	0 0 1	$1_{0\,1}$	A1	0,968	3871,38	0 2 0	$1_{1\,1}$	3871,30	0 2 0	$1_{1\,1}$	A2	0,990
2128,70	0 0 1	$1_{1\,1}$	2128,66	0 0 1	$1_{1\,1}$	B2	0,980	3881,70	0 2 0	$1_{1\,0}$	3881,63	0 2 0	$1_{1\,0}$	B2	1,000
2133,50	0 1 0	$3_{0\,3}$	2133,45	0 1 0	$3_{0\,3}$	B1	0,894	3909,91	0 2 0	$2_{0\,2}$	3909,84	0 2 0	$2_{0\,2}$	A1	0,974
2136,24	0 0 1	$1_{1\,0}$	2136,21	0 0 1	$1_{1\,0}$	A2	1,000	3921,97	0 2 0	$2_{1\,2}$	3921,89	0 2 0	$2_{1\,2}$	B2	0,966
2136,50	0 1 0	$3_{1\,3}$	2136,44	0 1 0	$3_{1\,3}$	A2	0,882	4058,48	0 0 2	$1_{0\,1}$	4058,42	0 0 2	$1_{0\,1}$	B1	0,847
2145,62	0 1 0	$2_{2\,1}$	2145,58	0 1 0	$2_{2\,1}$	B1	0,944	4062,89	0 0 2	$1_{1\,1}$	4062,83	0 0 2	$1_{1\,1}$	A2	0,757
2149,56	0 1 0	$2_{2\,0}$	2149,52	0 1 0	$2_{2\,0}$	A1	0,938	4097,09	0 0 2	$2_{0\,2}$	4097,00	0 0 2	$2_{0\,2}$	A1	0,758
2194,06	0 0 1	$2_{0\,2}$	2194,03	0 0 1	$2_{0\,2}$	B1	0,916	4097,90	0 0 2	$2_{1\,2}$	4097,84	0 0 2	$2_{1\,2}$	B2	0,748
2202,78	0 0 1	$2_{1\,2}$	2202,74	0 0 1	$2_{1\,2}$	A2	0,874	4101,08	0 0 2	$1_{1\,0}$	4101,01	0 0 2	$1_{1\,0}$	B2	1,000
2205,80	0 1 0	$3_{1\,2}$	2205,76	0 1 0	$3_{1\,2}$	B2	0,969	4119,11	0 1 1	$1_{1\,0}$	4119,07	0 1 1	$1_{1\,0}$	A2	1,000
2225,16	0 0 1	$2_{1\,1}$	2225,12	0 0 1	$2_{1\,1}$	B2	0,941	4122,95	0 1 1	$1_{0\,1}$	4122,90	0 1 1	$1_{0\,1}$	A1	0,756
2236,36	0 1 0	$3_{2\,2}$	2236,32	0 1 0	$3_{2\,2}$	A1	0,911	4130,79	0 1 1	$1_{1\,1}$	4130,75	0 1 1	$1_{1\,1}$	B2	0,849
2253,05	0 1 0	$3_{2\,1}$	2253,01	0 1 0	$3_{2\,1}$	B1	0,905	4179,77	0 1 1	$2_{1\,1}$	4179,72	0 1 1	$2_{1\,1}$	B2	0,769
2254,67	0 0 1	$2_{2\,1}$	2254,64	0 0 1	$2_{2\,1}$	A1	0,985	6482,03	1 2 0	$1_{1\,1}$	6481,96	1 2 0	$1_{1\,1}$	A2	0,990
2257,58	0 0 1	$2_{2\,0}$	2257,56	0 0 1	$2_{2\,0}$	B1	0,995	**6524,93**	**1 2 0**	**$1_{0\,1}$**	**6465,95**	**1 2 0**	**$1_{0\,1}$**	**B1**	**0,990**
2297,58	0 0 1	$3_{0\,3}$	2297,54	0 0 1	$3_{0\,3}$	A1	0,836	**6570,87**	**1 2 0**	**$2_{1\,2}$**	**6538,40**	**1 2 0**	**$2_{1\,2}$**	**B2**	**0,950**
2306,74	0 0 1	$3_{1\,3}$	2306,70	0 0 1	$3_{1\,3}$	B2	0,782	**6734,41**	**1 0 2**	**$2_{0\,2}$**	**6567,70**	**1 0 2**	**$2_{0\,2}$**	**A1**	**0,846**

II.2.6. Concluding remarks

As a summary to Sec. II.2., we conclude that in order to assign rovibrational quantum labels within the framework of the D^{2}FOPI program suite in a theoretically rigorous manner, the D^{2}FOPI package was extended with a code utilizing the RRD protocol. Motivated by this work, a detailed numerical investigation was carried out on the embedding dependence of the RRD scheme.

As one would expect, the numerical comparison of RRD overlaps for H_2O in the different embeddings shows the superiority of the Eckart embedding, *i.e.*, Eckart-based RRD overlaps exhibit less mixing than those corresponding to the other two embeddings. The bisector embedding performs slightly better than the R_1 embedding, at least for the water molecule.

Irrespective of the embedding employed, the RRD tables yield unambiguous labels for the overwhelming majority of the eigenstates in the lower-energy end of the spectrum. However, the RRD scheme starts breaking down at higher excitation energies and for higher J values. Numerical results clearly show that the RRD scheme provides considerably more unambiguous labels for rotations than the NMD scheme is able to do for vibrations, which suggests that the rigid-rotor approximation holds better for rotations than the normal-mode approximation for vibrations.

Based on Fig. 6, several labels in the BT2 linelist[54] of $H_2{}^{16}O$ might be problematic, since they disagree with clear assignments obtained from the RRD protocol.

When comparing RRD assignments with results from the active database approach of MARVEL[42] for the H_2D^+ and D_2H^+ molecules, the RRD algorithm proved to be a useful tool for validating experimental energy values and quantum labels, along with identifying some problematic cases probably originating from improper previous experimental assignment.

II.3. On the DVR of essential singularities

In many practical applications, *e.g.*, during the computation of the energy levels of Coulombic systems,[66,67] energy levels of the spherical oscillator,[5] quantum dynamics studies,[68] and during the computation of (ro)vibrational spectra of molecules employing internal coordinates,[10,5,69] singular terms in the Hamiltonian[10,70,71,72] have to be confronted. A common singular term, also present in most of the above-mentioned examples, is the term r^{-2} with $r \in [0,\infty)$. If one is to compute (ro)vibrational spectra up to or beyond dissociation, one might need to deal with wave functions not vanishing at singular geometries, which could lead to numerical difficulties arising from the singular operator terms. Partly motivated by failures of certain DVR schemes to treat singularities, several useful alternative strategies have been advanced for treating singularities in grid-based applications.[69,70,73,74,75,76] These approaches are not discussed here. It is more relevant for the present section to note that when applying the diagonal DVR approximation for the calculation of matrix elements of r^{-2}, numerical computations show in some cases accurate results with fast convergence.[5,77]

II.3.1. The case of a complete basis set

Assuming a complete set of basis functions, it is straightforward to demonstrate the validity of applying the quadrature approximation (diagonal DVR approximation) for singular operators of the form r^{-n} with $n \in \{1,2,...\}$ and $r \in [a,b]$. What needs to be shown is that the matrices of the singular operators are diagonal in the DVR representation, which can be thought of as a unitary transformation method,[78,79] *i.e.*, the DVR representation can be obtained by the transformation arising from changing the basis to the eigenvectors of the coordinate matrix. The diagonal form of the singular operators in the DVR can be proven by showing that the matrices of the singular operators are the powers of the inverse of the coordinate operator matrix, since a matrix and its inverse, and the powers of its inverse, share the same set of eigenvectors.

For $n = 1$ this can be shown as follows. Let $\mathbf{Q}_{ij} = \langle i | x | j \rangle$ and $\mathbf{R}_{ij} = \langle i | x^{-1} | j \rangle$ where $|i\rangle$ is the *i*th basis function, *x* is the coordinate operator, and $\langle f | g \rangle$ is the usual inner product between the elements *f* and *g* defined in the Hilbert space of the given quantum mechanical system. Assuming an orthonormal basis and using the identity relation $\hat{I} = \sum_{k=1}^{\infty} |k\rangle\langle k|$

$$(\mathbf{QR})_{ij} = \sum_{k=1}^{\infty} Q_{ik} R_{kj} = \sum_{k=1}^{\infty} \langle i|x|k\rangle\langle k|x^{-1}|j\rangle = \langle i|xx^{-1}|j\rangle = \langle i|j\rangle = \delta_{ij} = \mathbf{I}_{ij}.$$

Thus, **R** is the inverse of **Q**, therefore, they have the same eigenvectors, and **R** is diagonal in the DVR. For $n>1$ the following can be said. Let $\mathbf{R}_{ij}^{(n)} = \langle i|x^{-n}|j\rangle$. Assuming an orthonormal basis, $\mathbf{R}_{ij}^{(n)} = \langle i|x^{-n}|j\rangle = \sum_{k_1,k_2,k_3,\ldots,k_n=1}^{\infty} \mathbf{R}_{ik_1}\mathbf{R}_{k_1k_2}\mathbf{R}_{k_2k_3}\ldots\mathbf{R}_{k_nj} = \left(\mathbf{R}^n\right)_{ij}$

holds and the matrices of the singular operators with $n>1$ are the powers of **R.** Thus, they also have the same eigenvectors as the coordinate matrix **Q** and they are diagonal in the DVR.

II.3.2. The case of incomplete basis sets

When using an incomplete basis set of *N* functions, the approach of the previous section is not feasible, because $\hat{I} \neq \sum_{k=1}^{N} |k\rangle\langle k|$. However, following the idea of Dickinson and Certain[78] as reviewed, for example, by Light and Carrington,[6] one can provide an approximation to the error arising from the use of diagonal DVR matrices.

Let us take the set of $\{P_l(x)\}_{l=0}^{N-1}$ functions, defined in the $[a,b]$ interval of the coordinate, which are normed and orthogonal with respect to the real weight function $w(x)$. Let us also assume for the set of functions to have a corresponding quadrature with quadrature points $\{\lambda_i\}_{i=1}^{N}$ and real quadrature weights $\{w_i\}_{i=1}^{N}$, which are exact in representing the orthogonality of the above functions, *i.e.*,

$$\int_a^b w(x)P_k^*(x)P_l(x)dx = \sum_{i=1}^{N} w_i P_k^*(\lambda_i)P_l(\lambda_i) = \delta_{kl}. \qquad (14)$$

A straightforward example for $\{P_l(x)\}_{l=0}^{N-1}$ is a set of the first *N* of some classical orthogonal polynomials[80] defined in the interval $[a,b]$, with $\{\lambda_i\}_{i=1}^{N}$ and $\{w_i\}_{i=1}^{N}$ arising from the corresponding Gaussian quadrature rules. In this case the integrals calculated with the quadrature are exact for integrands of $w(x)$ weight function times a polynomial of order up to $2N-1$.

A useful and practical way for obtaining a set of quadrature points for a given orthonormal basis is to diagonalize the coordinate matrix.

To move forward, let our incomplete basis set of N functions be defined as $\left\{\phi_l(x)=\sqrt{w(x)}P_l(x)\right\}_{l=0}^{N-1}$. Then, the exact matrix elements (VBR representation) of the $f(x)$ operator are

$$\mathbf{F}_{kl}^{VBR}=\int_a^b \phi_k^*(x)f(x)\phi_l(x)dx$$

The approximate matrix elements (FBR representation) calculated within the quadrature approximation are

$$\mathbf{F}_{kl}^{FBR}=\sum_{i=1}^{N}\frac{w_i}{w(\lambda_i)}\phi_k^*(\lambda_i)f(\lambda_i)\phi_l(\lambda_i)$$

while the matrix elements in the diagonal DVR approximation are

$$\mathbf{F}_{kl}^{DVR}=f(\lambda_k)\delta_{kl}\,.$$

Let us define the matrix $\mathbf{T}_{sl}=\left[w_s/w(\lambda_s)\right]^{1/2}\phi_l(\lambda_s)\in\mathbb{C}^{N\times N}$ which is unitary if Eq. (14)

holds, since

$$\left(\mathbf{TT}^{+}\right)_{ij}=\sum_{s=1}^{N}\mathbf{T}_{is}\mathbf{T}_{js}^{*}=\sum_{s=1}^{N}\frac{w_s}{w(\lambda_s)}\phi_i(\lambda_s)\phi_j^*(\lambda_s)=\sum_{s=1}^{N}w_s P_i(\lambda_s)P_j^*(\lambda_s)=\int_a^b w(x)P_j^*(x)P_i(x)dx=\delta_{ij}.$$

With the help of the **T** matrix and a little algebra, one can derive the following relation,

$$\mathbf{F}_{ij}^{DVR}=f(\lambda_i)\delta_{ij}=\sum_{s=1}^{N}f(\lambda_s)\delta_{is}\delta_{js}=\sum_{s=1}^{N}f(\lambda_s)\left(\mathbf{TT}^{+}\right)_{is}\left(\mathbf{T}^{+}\mathbf{T}\right)_{js}=\sum_{s,k,l=1}^{N}f(\lambda_s)\mathbf{T}_{ik}(\mathbf{T}^{+})_{ks}(\mathbf{T}^{+})_{jl}\mathbf{T}_{ls}=$$

$$=\sum_{s,k,l=1}^{N}f(\lambda_s)\mathbf{T}_{ik}\mathbf{T}_{sk}^{*}\mathbf{T}_{jl}^{*}\mathbf{T}_{sl}=\sum_{k,l=1}^{N}\mathbf{T}_{jl}^{*}\mathbf{T}_{ik}\sum_{s=1}^{N}f(\lambda_s)\mathbf{T}_{sk}^{*}\mathbf{T}_{sl}=\sum_{k,l=1}^{N}\mathbf{T}_{jl}^{*}\mathbf{T}_{ik}\sum_{s=1}^{N}\frac{w_s}{w(\lambda_s)}\phi_k^*(\lambda_s)f(\lambda_s)\phi_l(\lambda_s)=$$

$$=\sum_{k,l=1}^{N}\mathbf{T}_{jl}^{*}\mathbf{T}_{ik}\mathbf{F}_{kl}^{FBR}=\left(\mathbf{TF}^{FBR}\mathbf{T}^{+}\right)_{ij}\,.$$

Thus, the FBR is a unitary transform of the diagonal DVR, the eigenvalues are the same in the two representations. This means that during the computation of the eigenvalues the error of the diagonal approximation using N basis functions is equivalent to the error arising from calculating the matrix element integrals with an N-point quadrature.

II.3.3. Test computations

In nuclear motion Hamiltonians singularities arise when building an internal coordinate system on a manifold. Where the Jacobian of the transformation vanishes, certain members of the coordinate system won't exist. If the wave function does not vanish at a

singular geometry (where the Jacobian vanishes) than the wave function is in the wrong space. However, as shown below, this may not cause unsurmountable difficulties for the actual nuclear motion computations.

As perhaps first discussed in Ref. 10, if the wave function becomes vanishingly small nearby a singular geometry, it is possible to deal with singular terms by suitable schemes of numerical integration or with a choice of a suitable DVR, whereby points in the vicinity of the singularity are avoided during computation of the singular matrix elements. If, however, the wave function does not vanish at the singular geometry, the situation becomes somewhat more difficult, as is the case for the H_3^+ molecular ion when the vibrations are treated in the Jacobi coordinate system and the molecule samples linear configurations.

Sample computations concerning the singular term r^{-2} with $r \in [0,\infty)$ often arising in practical applications have been performed in one and three dimensions. Eigenenergies for the spherical oscillator model problem (1-D) and for the vibrational energies of the H_3^+ molecule (3-D) show that when basis functions with proper boundary conditions *i.e.*, satisfying the boundary conditions implied by the given physical system, are used, the diagonal DVR approximation is suitable to get converged eigenstates. The 1-D case is treated in detail in Ref. 5 so it is not discussed further here.

Some relevant numerical results for the vibrational energies of the H_3^+ molecular ion are presented in Figure 7, obtained using the Hamiltonian given in Eq. (1) and the corresponding volume element. The 3-D test computations[5] of the vibrational energy levels up to near dissociation were carried out using the D^{2}FOPI code applying Jacobi coordinates and a basis set of potential optimized (PO)[12,13,14] Bessel-DVR basis functions for the stretching-type coordinates and Legendre polynomials for the angle-type coordinate. This choice of the Hamiltonian, volume element, and basis functions, exhibiting the appropriate boundary conditions, ensures that (a) the eigenfunction (wave function times the stretching coordinates) vanishes at the singularity; and (b) the numerical procedure yields correct eigenvalues. Fig. 7 shows the absolute error of non-converged even-parity vibrational energy levels, with respect to the converged results, obtained either via computing all the matrix elements of the r^{-2} radial singular terms analytically or via using the diagonal DVR approximation. As can be seen in Fig.7, the error of the vibrational eigenenergies are nearly identical in the two cases, the diagonal DVR approximation can be used for the evaluation of singular operator matrix elements. This general result can be of great help to reduce the cost of computations limited by computer power, such as (ro)vibrational calculations on larger molecules.

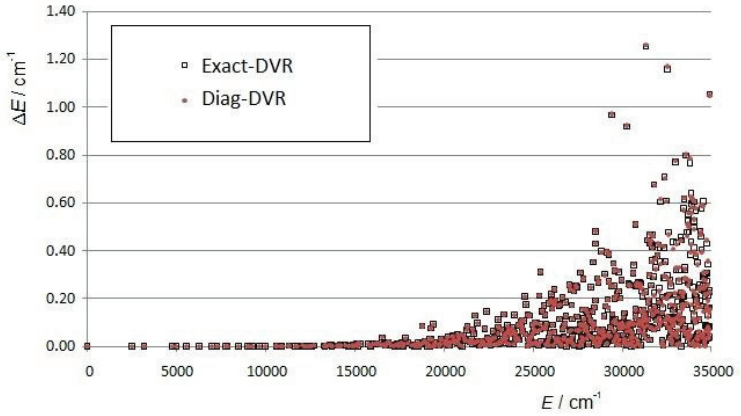

Figure 7. Pictorial representation of the convergence of the even-parity vibrational states of the H_3^+ molecule. The computations were performed with (Diag-DVR) or without (Exact-DVR) using the diagonal DVR approximation for the r^{-2} singular terms in the Jacobi coordinate system and employed 105 and 100 PO Bessel-DVR functions for the two distance-type and 35 Legendre basis functions for the angle-type coordinates. Absolute deviations from the fully converged eigenenergies obtained with 120, 120, and 51 basis functions applying the Exact-DVR technique are shown.

As detailed above, the error in the eigenvalues obtained with the diagonal DVR approximation are almost identical with the error of eigenvalues obtained in the FBR using Gaussian quadrature for evaluating matrix elements. Table 5 presents the case of spherical-oscillator basis functions[5] which have the same boundary conditions as the PO Bessel-DVR functions, *i.e.*, boundary conditions such that the integrands in the integrals defining the matrix elements of the r^{-2} singular operator are not singular. However, when one uses Gaussian quadrature for computing the integrals it is necessary to defactor the weight function of the Gaussian quadrature, which in turn causes the integrand to become singular. As expected, the matrix elements of the r^{-2} singular operator obtained in the FBR through Gaussian quadrature have large relative errors with respect to the VBR. Nevertheless, the eigenvalues show much less deviation from the VBR eigenvalues. This observation is related

to the applicability of the diagonal DVR approximation for evaluating matrix elements of the r^{-2} singular term.

Due to the wide range of applications, and possibly also to provide insight into other possible approximations which are not considered otherwise, it would be of great general interest to have a rigorous mathematical explanation for the applicability of the diagonal DVR approximation for evaluating matrix elements of the r^{-2} singular term. This is clearly an important field for future research.

Table 5. Average relative errors, in %, of the eigenvalues and matrix elements of the singular operator r^{-2} with $r \in [0,\infty)$ in an FBR, obtained with Gaussian approximation, taken with respect to the appropriate VBR values.

Eigevalues	Matrix elements									
0.6	26	39	50	59	67	74	80	86	92	97
0.7	39	41	50	59	67	74	80	86	92	97
0.9	50	50	52	59	67	74	80	86	92	97
1.1	59	59	59	60	67	74	80	86	92	97
1.4	67	67	67	67	68	74	80	86	92	97
1.8	74	74	74	74	74	75	80	86	92	97
2.4	80	80	80	80	80	80	81	86	92	97
3.5	86	86	86	86	86	86	86	87	92	97
6.1	92	92	92	92	92	92	92	92	93	97
25.1	97	97	97	97	97	97	97	97	97	98

Matrix elements of the singular operator were computed using 100 basis functions based on spherical oscillator functions. The values presented in the table were obtained through averaging every 10 eigenvalues and the "corresponding" 10 X 10 matrix elements.

III. Energy levels beyond dissociation

III.1. What are resonance states?

Resonance states, also known as quasi-bound states, of a system are metastable states which have sufficient energy to brake up the system into its subsystems. They decay exponentially with time. Though seldom considered, they play an important role in atomic and molecular physics,[81,82,83,84] for example, in unimolecular reactions, in photodissociation and photoassociation studies, and in scattering phenomena.

Although a well-founded, rigorous mathematical theory of resonance states is available,[85,86] it requires an in-depth knowledge of functional analysis which is usually beyond the scope of everyday theoretical chemists. For a variety of practical applications, however, it seems that an intuitive approach to resonance phenomena is sufficient. For example, following the approach of Refs. 87 and 88, in the Schrödinger representation resonance states can be associated with outgoing eigenfunctions of the Hamiltonian, diverging exponentially at infinity. Due to the outgoing boundary condition, the eigenvalues corresponding to resonance states are complex. They are usually written as $E_n^{\mathrm{res}} = \varepsilon_n - \frac{i}{2}\Gamma_n$, where ε_n is the resonance position and Γ_n is the width (inverse lifetime) of the resonance state. Let us review how one "derives" resonance states in a compact and intuitive theoretical manner. For simplicity the resonances of a single particle in a time-independent central potential will be discussed, generalizations will be given later. Detailed discussion of some of the steps will be omitted, as it is mainly elementary textbook material.[87]

Having a $\hat{H}$ time-independent Hamiltonian, we are looking for the stationary solutions of the time-dependent Schrödinger-equation

$$i\hbar\frac{\partial\Psi(\mathbf{r},t)}{\partial t} = \hat{H}\Psi(\mathbf{r},t) \tag{15}$$

i.e., the wavefunction is sought in a product form

$$\Psi(\mathbf{r},t) = \psi(\mathbf{r})T(t) \tag{16}$$

which leads to the well-known equations

$$T(t) = e^{-\frac{i}{\hbar}Et} \tag{17}$$

and

$$\hat{H}\psi(\mathbf{r}) = E\psi(\mathbf{r}). \tag{18}$$

Writing out the Hamiltonian explicitly and rearranging Eq. (18), we arrive at

$$\left(-\frac{\hbar^2}{2m}\Delta + V(r) - E\right)\psi(\mathbf{r}) = 0 \tag{19}$$

where m is the mass of the particle, Δ is the Laplacian, and $\hbar$ is the reduced Planck constant. With further arrangement and by introducing the variables $k^2 = \frac{2m}{\hbar^2}E$ and $U(r) = \frac{2m}{\hbar^2}V(r)$, Eq. (19) can be written as

$$\Delta\psi(\mathbf{r}) + \left(k^2 - U(r)\right)\psi(\mathbf{r}) = 0 \tag{20}$$

At this point, changing to spherical coordinates and with the further use of the separation of variables via $\psi(\mathbf{r}) = R(r)Y(\vartheta,\varphi)$, where r is the distance from the origin while ϑ and φ are the usual spherical angles, one arrives at a series of one-dimensional radial equations

$$\frac{\partial^2\chi_l(r)}{\partial r^2} + \left(k^2 - U(r) - \frac{l(l+1)}{r^2}\right)\chi_l(r) = 0 \quad , l \in \{0,1,2,...\} \tag{21}$$

along with $\psi(\mathbf{r}) = \frac{1}{r}\chi_l(r)Y_l^m(\vartheta,\varphi)$ such that $\chi_l(r) = R_l(r)/r$ and $Y_l^m(\vartheta,\varphi)$ are the usual spherical harmonics.

The asymptotic form of Eq. (21) is

$$\frac{\partial^2\chi_l^{(a)}(r)}{\partial r^2} + k^2\chi_l^{(a)}(r) = 0 \quad , l \in \{0,1,2,...\} \tag{22}$$

for which the general solution is

$$\chi_l^{(a)}(r) = A_l(k)e^{ikr} + B_l(k)e^{-ikr}, \tag{23}$$

which incorporates three vastly different situations according to the boundary conditions one demands for the solutions of Eq. (21). These are as follows.

a) For bound states, one demands that the wavefunctions are in the Hilbert-space (which means $\chi \in L^2\left(\mathbb{R}^+\right)$ for Eq. (21)), thus χ must be L^2 normalizable. In the Hilbert-space domain the Hamiltonian is hermitian, its eigenvalues are real. The required boundary conditions can be met by $E < 0$ which means k is pure imaginary and can be written as $k = i\lambda,\ \lambda \in \mathbb{R}\setminus\{0\}$, which results that from the asymptotic form in Eq. (23) only the factor of the first term (only $\lambda > 0$ case is considered, $\lambda < 0$ is essentially the same) can be non-zero in order for the wavefunction to be square integrable, thus we get

$$\chi_l^{(a)}(r) = A_l(k)e^{-\lambda r}. \tag{24}$$

This is the well-known exponentially decaying asymptotic behavior for bound states.

b) Although, strictly speaking, scattering states are not in the Hilbert space,[85] with Dirac's bra-ket formalism formally they can be treated as such, and since they are not square integrable (not L^2 normalizable) in practice they are "Dirac-delta normalized". So for scattering states one requires the wavefunction to be finite at infinity and Dirac-delta normalizable, which can be achieved with positive real energy eigenvalues, *i.e.*, for $E > 0$ k is real, and the two terms in Eq. (23) correspond to the outgoing and incoming sphere waves (or plane waves for a one-dimensional problem), respectively.

c) For resonance states, one searches for boundary conditions and corresponding energy eigenvalues that describe a system that falls into its subsystems, *i.e.*, has outgoing boundary conditions with no incoming wave term in Eq. (23) ($B_l(k) = 0$ for resonance states), and the decay follows an exponential rule in time. Looking at Eq. (17), it is clear that the exponential decay in time, which is a characteristic attribute of resonance states, can only be achieved with complex energy eigenvalues, which can be written as $E^{\text{res}} = \varepsilon - \frac{i}{2}\Gamma$, where ε is associated with the resonance position and (as will be seen later) Γ is the width (inverse lifetime) of the resonance state. It is noted that although for a Hamiltonian to have complex eigenvalues might be surprising at first, it is quite natural if one considers that wavefunctions which have outgoing boundary conditions are not in the Hilbert-space, *i.e.*, they are not in the self-adjoint domain of the Hamiltonian. The asymptotic form of the resonance radial function of Eq. (23) is

$$\chi_l^{(a)}(r) = A_l(k)e^{ikr} = A_l(k)e^{iar}e^{br}, \tag{25}$$

where

$$a = \left(\frac{2m}{\hbar^2}\right)^{1/2}\left(\varepsilon^2 + (\Gamma/2)^2\right)^{1/4}\cos(\varphi),$$

$$b = a\tan(\varphi),$$

$$\varphi = \frac{1}{2}\arctan(\Gamma/2\varepsilon).$$

Using these expressions the asymptotic form of the complete wavefunction of the system is written as

$$\Psi_l^{(a)}(\mathbf{r},t)=\psi_l^{(a)}(\mathbf{r})T(t)=\frac{1}{r}\chi_l^{(a)}(r)Y_l^m(\phi,\theta)e^{-\frac{i}{\hbar}Et}=$$
$$=Y_l^m(\phi,\theta)\frac{A_l(k)}{r}e^{iar}e^{br}e^{-\frac{i}{\hbar}\left(\varepsilon-i\frac{\Gamma}{2}\right)t}=Y_l^m(\phi,\theta)\frac{A_l(k)}{r}e^{iar}e^{br}e^{-\frac{i}{\hbar}\varepsilon t}e^{-\frac{\Gamma}{2\hbar}t}= \tag{26}$$
$$=Y_l^m(\phi,\theta)\frac{A_l(k)}{r}e^{i\left(ar-\frac{\varepsilon}{\hbar}t\right)}e^{br}e^{-\frac{\Gamma}{2\hbar}t}$$

From Eq. (26) one can see how Γ is related to the inverse lifetime of the system and that in order to have exponential decay in time, $\Gamma>0$ must hold, which, along with $\varepsilon>0$ (the system is assumed to have energy higher than the dissociation energy which is zero in our example), leads to $b>0$, which means that the wavefunction diverges exponentially as $r\to\infty$.

A physical interpretation of the divergence property of the wavefunction can be that at $r\to\infty$ one observes the particles which were formed an infinitely long time ago.[87]

Generalization of the results obtained for the simple model system detailed above to larger quantum systems can be achieved quite straightforwardly by interpreting *r* as a dissociation coordinate, or in other words interpreting *r* as the "reaction" coordinate corresponding to the dissociation of the system.

In summary, the resonance states of a quantum system are associated with stationary states which have wave functions diverging exponentially with respect to the dissociation coordinate(s) *r*, and have energy eigenvalues of the form $E^{\text{res}}=\varepsilon-\frac{i}{2}\Gamma$, with $\Gamma>0$ and $\varepsilon>E_d^r$, where E_d^r is the dissociation threshold corresponding to the dissociation channel described by the *r* "reaction" coordinate.

Due to their diverging asymptotic behavior, resonance wave functions are not square integrable; thus, one would think at first that the L^2 methods discussed in the earlier sections of this thesis are not suitable for describing them. There are, however, several methods available which do make possible the determination of resonance eigenstates using L^2 methods, usually based on employing modified non-Hermitian Hamiltonians whose eigenvalues with corresponding L^2 eigenfunctions can be used for evaluating or approximating resonance positions and widths. The two most popular methods are the complex coordinate (CC) method[88, 89, 90] and the complex absorbing potential (CAP) method.[91,92,93] The latter seems to be favored for calculating (ro)vibrational resonances of

polyatomic molecules.[94,95,96,97,98] Recent works[94,97,98] exploited efficient numerical techniques corresponding to well-developed L^2 methods for computing resonance eigenvalues.

Experimentally observed, near-threshold resonance structures of the spectra of molecules have mostly defied detailed first-principles analysis.[99,100] Nevertheless, it is clear that there are at least two well-defined mechanisms that lead to the formation of long-lived resonances. Rotational excitation of below-threshold vibrational states leads to a centrifugal barrier, behind which high-energy rovibrational states can be trapped temporarily, giving rise to so-called shape resonances. The width of shape resonances is determined by the centrifugal barrier. Shape resonances can extend to hundreds of wavenumbers above the dissociation threshold and they result in narrow features in the spectrum due to their tunneling character. These resonances are responsible, for example, for part of the famous Carrington bands, the multitude of still unassigned lines observed in the near-dissociation spectrum of H_3^+.[99] Vibrational excitation into high-energy states which do not lead toward dissociation gives Feshbach (sometimes called Feshbach-Fano) resonances. Both types of resonances have been identified in the near-threshold spectrum of the water vapor.[3,101] A combination of these two mechanisms has also been observed.[96] It is expected that as the method developments continue resonance-state computations will become widespread for 3-5-atomic systems, extending our knowledge[95,102,103,104,105,106,101] about them.

III.2. Computing resonance states in quantum chemistry

III.2.1. Complex Absorbing Potential (CAP) method

In the CAP method, the Hermitian Hamiltonian is perturbed with a complex absorbing potential, which damps the outgoing wave functions at the asymptotic region of the PES, making them square integrable and suitable for an L^2 basis expansion.

Considering only imaginary CAPs, the perturbed Hamiltonian might be written as

$$\hat{H}(\eta) = \hat{H} - i\eta W(r) \tag{27}$$

where $W(r)$ is a real valued function of the dissociation coordinate(s) r giving the functional form of the CAP, while the strength of the absorbing potential can be set with the real parameter η.

The perturbation of the Hamiltonian with a CAP naturally changes the eigenvalues along with damping the eigenfunctions. The change of the resonance eigenvalues caused by the CAP can be written[92] as a power series of η, *i.e.*, for a given E^{res} resonance eigevalue

$$E(\eta) = E^{\mathrm{res}} + a_1\eta + a_2\eta^2 + \ldots \tag{28}$$

where $E(\eta)$ is the corresponding eigenvalue of the perturbed Hamiltonian. Eq. (28) would be the case if one calculated eigenvalues exactly. In practical applications, however, one uses a finite basis set, which introduces an error; therefore, the $E^{\mathrm{fb}}(\eta)$ computed eigenvalues of the perturbed Hamiltonian may be written as

$$E^{\mathrm{fb}}(\eta) = E^{\mathrm{res}} + a_1\eta + a_2\eta^2 + \ldots + g(\eta), \tag{29}$$

where $E^{\mathrm{fb}}(\eta)$ is the eigenvalue of the perturbed Hamiltonian computed in a finite basis and $g(\eta)$ is the basis set error. Thus, when one computes the eigenvalues of the Hamiltonian perturbed by a CAP, one faces two error terms with respect to the exact resonance eigenvalue. The first error term is the power series in η which naturally increases, as one increases the CAP strength parameter η. The second error term $g(\eta)$, on the other hand, decreases as η is increased, since a stronger CAP damps the resonance wavefunctions more strongly, making them easier to expand in an L^2 basis, which leads to smaller $g(\eta)$ basis set error. Therefore, within a single resonance state, as one changes the CAP strength parameter η from a "very small" value to a "very large" value, and while doing so plots the computed $E^{\mathrm{fb}}(\eta)$ eigenvalue, one obtains a trajectory on the complex plane. Around one end of the trajectory, where η is "large", the power series error is dominant, while around the other end, where η is "small", the basis set error is dominant. Somewhere in between the two cases is the point on the trajectory where the two errors are equal, and which is the best approximation for the exact resonance eigenvalue.[92] Since the power series error and the basis set error (which are complex valued functions of the η parameter) approach the point of best approximation with different phases,[92] one can observe a cusp in the eigenvalue trajectory around the point of best approximation.

Thus, along with other alternatives not detailed here,[92,94,97] resonance eigenvalues in the CAP method can be evaluated[92,94,98] by finding cusps in eigenvalue trajectories obtained by diagonalizing the complex symmetric Hamiltonian matrix with different CAP parameters.

III.2.2. D^{2}FOPI and the CAP method

Motivated by the success and popularity of the CAP method in the literature, a program was developed for computing resonance energies within the CAP method based on D2FOPI computations. Following the work of Ref. 98, the algorithm can be described as follows:

1) Bound states up to dissociation and many eigenvectors with energies above the dissociation energy are computed using the D^{2}FOPI program, *i.e.*,

$$\hat{H}\Psi_k = E_k\Psi_k, \quad k \in \{1,2,...,N\} \tag{30}$$

is solved, where $\hat{H}$ is the triatomic (ro)vibrational Hamiltonian and N is larger than the number of bound states.

2) Using a subset of the Ψ_k, $k \in \{1,2,...,N\}$, computed eigenvectors as a basis, the matrix representation of the CAP-modified Hamiltonian,

$$\hat{H}(\eta) = \hat{H} - i\eta W(r),$$

is constructed via

$$\mathbf{H}_{kl} = E_k\delta_{kl} - i\eta\left\langle \Psi_k \middle| \hat{W} \middle| \Psi_l \right\rangle \tag{31}$$

and its eigenpairs are computed for a great many values of the CAP parameter η. In other words, at each step, while varying the CAP strength, the perturbed Hamiltonian matrix is constructed and diagonalized, and the resulting eigenpairs are stored.

3) As a function of the CAP strength parameter, the eigenvalues of the CAP-perturbed Hamiltonian are plotted, resulting in a set of N eigenvalue trajectories on the complex plane, which are then analyzed by an automatic procedure, which detects cusps in the trajectories. If a cusp is present near the same position for a majority of different CAP functions used, *i.e.*, the cusp position is independent of the functional form of the CAP, it is associated with a resonance eigenvalue.

Construction of the eigenvalue trajectories (after each CAP strength parameter changing step, pairing up the eigenvalues with the eigenvalues of the previous step) is done by computing eigenvector overlaps at each CAP strength changing step, *i.e.*, at each step each eigenvalue is associated with the eigenvalue of the previous step with which their eigenvectors give the largest overlap. It is noted that although this is not necessarily a clear procedure in the sense that the eigenvectors are not continuous functions of the matrix elements, in practice no discontinuous behavior was observed in the eigenvalue trajectories around the region of interest, only occasionally at "very small" η values.

The automated cusp detection is achieved by computing the curvature and point density along the trajectories and locating their local maxima. If somewhere along a trajectory (within some energy error threshold) both the curvature and the point density has a local maximum, that point is labeled as a cusp and stored. The well-known formula [107] for evaluating the curvature κ of a parameterized two dimensional curve reads in this case as

$$\kappa(\eta) = \frac{\frac{d\,\mathrm{Re}\left[E^{\mathrm{fb}}(\eta)\right]}{d\eta}\frac{d^2\,\mathrm{Im}\left[E^{\mathrm{fb}}(\eta)\right]}{d\eta^2} - \frac{d\,\mathrm{Im}\left[E^{\mathrm{fb}}(\eta)\right]}{d\eta}\frac{d^2\,\mathrm{Re}\left[E^{\mathrm{fb}}(\eta)\right]}{d\eta^2}}{\left(\left(\frac{d\,\mathrm{Re}\left[E^{\mathrm{fb}}(\eta)\right]}{d\eta}\right)^2 + \left(\frac{d\,\mathrm{Im}\left[E^{\mathrm{fb}}(\eta)\right]}{d\eta}\right)^2\right)^{3/2}}, \tag{32}$$

where differentiations with respect to the CAP strength parameter are carried out numerically by using simple finite differences. The point density is considered to be inversely proportional to the norm of the eigenvalue derivative with respect to the CAP strength parameter, which can be written as

$$\mathrm{DN}(\eta) = \left(\left(\frac{d\,\mathrm{Re}\left[E^{\mathrm{fb}}(\eta)\right]}{d\eta}\right)^2 + \left(\frac{d\,\mathrm{Im}\left[E^{\mathrm{fb}}(\eta)\right]}{d\eta}\right)^2\right)^{1/2} \tag{33}$$

where differentiations are also computed using simple finite differences.

III.2.3. Complex coordinate scaling

III.2.3.1. What is complex scaling?

The complex scaling method, also known as the complex rotation or complex coordinate method, has been a tool of computational chemistry and molecular physics for several decades. Excellent application-oriented reviews[88,89,90] can be found in the literature along with discourses on the rigorous mathematical foundations.[108,109,110,111] Over the years several variants of the "conventional" complex scaling method were proposed, such as the exterior complex scaling or the smooth exterior complex scaling, for example, from which one may obtain the CAP method by using certain approximations.[88] Let us review the basic idea behind using complex coordinates.

When the goal is to compute resonance positions, one is looking for solutions of the time-independent Schrödinger equation having wavefunctions with exponentially diverging asymptotic behavior.

$$\hat{H}\Psi^{\text{res}} = E^{\text{res}}\Psi^{\text{res}}, \quad \Psi^{\text{res}} \notin L^2 \tag{34}$$

Let us introduce an invertible operator $\hat{S}$ for obtaining a similarity transformation of the Schrödinger equation, *i.e.*,

$$\hat{S}\hat{H}\hat{S}^{-1}\hat{S}\Psi^{\text{res}} = E^{\text{res}}\hat{S}\Psi^{\text{res}} \tag{35}$$

Also let us choose the $\hat{S}$ operator so that the functions $\Phi \equiv \hat{S}\Psi^{\text{res}}$ are square integrable, *i.e.*,

$$\hat{S}\hat{H}\hat{S}^{-1}\Phi = E^{\text{res}}\Phi, \quad \Phi \in L^2. \tag{36}$$

Thus, we obtained an eigenvalue equation for the transformed Hamiltonian $\hat{S}\hat{H}\hat{S}^{-1}$, where the eigenvalues are the exact resonance eigenvalues, and the corresponding eigenfunctions are square integrable, thus can be computed with the well developed L^2 techniques.

As shown in the next section, for the exponentially diverging resonance wave functions a suitable definition for the transformation operator can be

$$\hat{S}_\theta f(r) = f(re^{i\theta}) \tag{37}$$

where θ is a free parameter. In words, the operator $\hat{S}_\theta$ rotates the argument of a function by θ in the complex plane. $\hat{S}_\theta$ can be utilized for analytical functions for example by

$$\hat{S}_\theta = e^{i\theta r\frac{\partial}{\partial r}}$$

since

$$\hat{S}_\theta f(r) = e^{i\theta r\frac{\partial}{\partial r}} f(r) = \lim_{N\to\infty}\left(\hat{I} + \frac{i\theta r}{N}\frac{\partial}{\partial r}\right)^N f(r) = \lim_{N\to\infty}\left(\hat{I} + \frac{i\theta r}{N}\frac{\partial}{\partial r}\right)^{N-1}\left(\hat{I} + \frac{i\theta r}{N}\frac{\partial}{\partial r}\right) f(r) =$$

$$= \lim_{N\to\infty}\left(\hat{I} + \frac{i\theta r}{N}\frac{\partial}{\partial r}\right)^{N-1}\left[f\left(r + \frac{i\theta r}{N}\right) + o\left(\frac{\theta^2 r^2}{N^2}\right)\right] = \lim_{N\to\infty}\left(\hat{I} + \frac{i\theta r}{N}\frac{\partial}{\partial r}\right)^{N-1}\left[f\left(\left(1 + \frac{i\theta}{N}\right)r\right) + o\left(\frac{\theta^2 r^2}{N^2}\right)\right] =$$

$$= \lim_{N\to\infty}\left[f\left(\left(1 + \frac{i\theta}{N}\right)^N r\right) + No\left(\frac{\theta^2 r^2}{N^2}\right)\right] = f\left(\lim_{N\to\infty}\left(1 + \frac{i\theta}{N}\right)^N r\right) = f\left(re^{i\theta}\right).$$

III.2.3.2. Effect of complex scaling on the asymptotic behavior of wave functions

Let's see the asymptotic behavior of the exponentially diverging radial function of Eq. (25) if acted upon by the operator $\hat{S}_\theta$ (which is the same as the asymptotic behavior of a general resonance wave function complex scaled in the reaction coordinate(s) in which the resonance wave function diverges exponentially):

$$\hat{S}_\theta \chi_l^{(a)}(r) \propto \hat{S}_\theta e^{iar} e^{br} = e^{iare^{i\theta}} e^{bre^{i\theta}} = e^{iar} e^{-\beta r} \tag{38}$$

where

$$\alpha = a\left(\cos(\theta) + \tan(\varphi)\sin(\theta)\right)$$
$$\beta = a\left(\sin(\theta) - \tan(\varphi)\cos(\theta)\right)$$
$$a = \left(\frac{2m}{\hbar^2}\right)^{1/2}\left(\varepsilon^2 + (\Gamma/2)^2\right)^{1/4}\cos(\varphi)$$
$$\varphi = \frac{1}{2}\arctan(\Gamma/2\varepsilon)$$

From Eq. (38) one can see that in order for the complex scaled radial function to be square integrable (or more generally, for scaled resonance wavefunctions to be square integrable) $\tan\theta > \tan\varphi$ must hold. Considering that $\varphi > 0$, upon scaling $\hat{S}_\theta$ only those resonance states will become square integrable for which $\theta > \varphi = \frac{1}{2}\arctan(\Gamma/2\varepsilon) = \frac{1}{2}Arg\left(E^{\text{res}}\right)$.

For bound states, it can be easily seen from Eq. (24) and also is known from the literature[88,89,108,109,110] that upon complex scaling, for Θ values of physical interest, *i.e.*, $\theta < \pi/4$, the bound states remain square integrable.

As for scattering states, they become divergent upon complex scaling for real *k* values in Eq. (23), but within the framework of the Balsev–Combes theorem[109] the scaled scattering wave functions contain also combinations of incoming and outgoing waves with bounded, non-square integrable (scattering) asymptotic behavior which are associated with a continuum that is rotated into the lower-half of the complex energy plane by the angle 2θ.[88,89]

Based on the asymptotic behavior of the wave functions of the complex scaled Hamiltonian discussed above, one can imagine a qualitative picture of the spectrum of the scaled Hamiltonian (within the Hilbert-space and the space of bounded, Dirac-normalizable functions), having real discrete eigenvalues for bound states, a scattering continuum rotated into the lower half of the complex plane by 2θ (for each dissociation channel) and discrete complex eigenvalues in the area between the real axis and the rotated scattering continua corresponding to resonance states. As a demonstration, the two panels of Fig. 8 show a) sketch of a spectrum of a complex-scaled Hamiltonian of a system with a single dissociation channel, and b) sketch of a spectrum of a complex-scaled Hamiltonian of a system having multiple dissociation channels computed using an L^2 method.

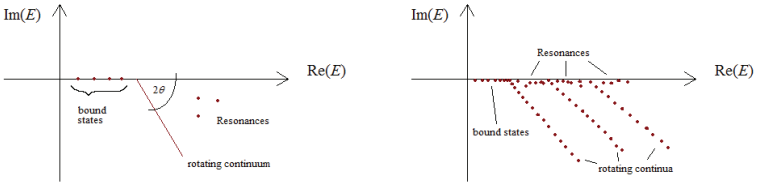

Figure 8. a) the spectrum of a complex scaled Hamiltonian of a system with a single dissociation channel and b) the spectrum of a scaled Hamiltonian of a system having multiple dissociation channels computed using L^2 methods

To conclude, for a resonance state satisfying Eq. (34) with wave functions having exponential asymptotic divergence with respect to the dissociation coordinate(s) and complex eigenvalue E^{res}, one may construct a complex-scaled Hamiltonian upon similarity transformation with the operator of Eq. (37), which naturally has the same E^{res} eigenvalue with corresponding square integrable wave functions as long as $\theta > \frac{1}{2} Arg\left(E^{\text{res}}\right)$ holds for the scaling parameter.

III.2.3.3. The complex scaled Hamiltonian

So far we have considered the effect of complex scaling on the boundary properties of different wave functions and thus qualitatively its effect on the spectrum. For applications, however, we need the actual form of the complex scaled Hamiltonian which is fortunately rather simple to obtain for the scaling operator of Eq. (37). The non-relativistic Hamiltonians of quantum mechanics are usually built from differential operators and functions of the coordinate operator(s), thus we only need to consider the complex scaling of this two types of operators.

Let r be the coordinate being scaled by the $\hat{S}_\theta f(r) = f(re^{i\theta})$ operator. The scaled form of the differential operator $\frac{\partial}{\partial r}$ then acts on an analytical function $f(r)$ as

$$\hat{S}_\theta \frac{\partial}{\partial r} \hat{S}_\theta^{-1} f(r) = \hat{S}_\theta \frac{\partial}{\partial r} f(re^{-i\theta}) = \hat{S}_\theta \frac{\partial f(re^{-i\theta})}{\partial (re^{-i\theta})} e^{-i\theta} = \hat{S}_\theta \frac{\partial f(re^{-i\theta})}{\partial r} e^{-i\theta} = \frac{\partial f(r)}{\partial r} e^{-i\theta} \qquad (39)$$

where we took advantage of the fact that $f(r)$ is analytic, thus its derivative with respect to r and $re^{-i\theta}$ are the same. As seen from Eq. (39), the differential operator $\frac{\partial}{\partial r}$ simply receives a

constant multiplier upon complex scaling. Derived in the same manner, it is easy to see that the differential operator $\frac{\partial^2}{\partial r^2}$ takes the form

$$\hat{S}_\theta \frac{\partial^2}{\partial r^2} \hat{S}_\theta^{-1} f(r) = \frac{\partial^2 f(r)}{\partial r^2} e^{-2i\theta} \tag{40}$$

upon complex scaling. As for the functions of the coordinate operator of the form $\hat{V}(r)$, which are multiplicative operators,

$$\hat{S}_\theta \hat{V}(r) \hat{S}_\theta^{-1} f(r) = \hat{S}_\theta \hat{V}(r) f(re^{-i\theta}) = \hat{S}_\theta V(r) f(re^{-i\theta}) = V(re^{i\theta}) f(r), \tag{41}$$

thus upon complex scaling formally they remain the same multiplicative operators, but multiply by functional values obtained at the scaled coordinate values.

To illustrate what was said above, for a simple one-dimensional Hamiltonian of the form

$$\hat{H} = -\frac{1}{2}\frac{d^2}{dr^2} + V(r), \quad V(r) = \frac{15}{2} r^2 e^{-r} \tag{42}$$

complex scaling gives

$$\hat{S}_\theta \hat{H} \hat{S}_\theta^{-1} = \hat{S}_\theta \left(-\frac{1}{2}\frac{d^2}{dr^2} + V(r) \right) \hat{S}_\theta^{-1} = -\frac{e^{-2i\theta}}{2}\frac{d^2}{dr^2} + \frac{15}{2} r^2 e^{2i\theta} e^{-re^{i\theta}} \tag{43}$$

III.2.3.4. Detecting resonance eigenstates in the complex coordinate formalism

In practical applications the question arises how one should identify resonance eigenvalues when using complex scaling. Naturally, resonance eigenvalues with physical meaning should be independent of the scaling parameter θ. However, in practice, when one uses finite basis sets, this is not necessarily true. By changing the scaling parameter, one changes the form of the wave functions, thus also changes the "goodness" of the basis. Therefore, the basis set error and hence the computed eigenvalues depend on the scaling parameter. It is known[89] and one can also see it in the examples of the applications section that for the bound states and resonance states (which already have square integrable wave functions at the given θ value), increasing θ makes it more difficult to expand the wave function in terms of an L^2 basis set due to the oscillatory term in Eq. (38). Two possible ways to identify resonance eigenvalues in calculations utilizing complex scaling are outlined below:

1) Looking at Fig. 8, the most natural way to identify resonance eigenvalues seems to be by plotting the computed spectrum and associating resonance states visually with the eigenvalues between the real axis and the rotated scattering continua. This might be a feasible

route if one has excellent basis set convergence, the computed points in the rotated continua form indeed a straight line and are clearly separable from the resonance eigenvalues. This is the case in the one-dimensional model systems discussed in the applications section. However, if basis set convergence (which also changes with θ) is barely met, then the computed points in the rotated continua form a straight line only approximately, or the spectra is dense and the resonance eigenvalues are not clearly separated from the points of the rotated continua, visual resonance identification from a single spectrum does not seem to be the proper choice as will also be seen in the section on triatomic vibrational resonances.

2) It is well known[112] that resonance eigenvalues can be identified in the complex scaling formalism by locating stationary points in eigenvalue trajectories obtained by varying the scaling parameter θ. In practice this can be achieved by computing the spectra of the scaled Hamiltonian for a large number of θ values and examining the eigenvalue trajectories numerically or visually.

III.2.4. D^{2}FOPI and the complex coordinate method

As seen in Eq. (41), in the complex coordinate framework one needs to evaluate the coordinate operators at complex values. For computing electronic resonances, where the potential energy function is given in terms of simple Coulombic potentials, complex scaling is trivial. The case is more difficult for computing polyatomic nuclear motion resonances, where scaling of the molecular potential energy surfaces (PES) is not necessarily an easy task. If an analytic fit of the PES is available, then complex scaling can be done by using the analytic form of the PES in complex arithmetic which usually requires the rewriting of the PES subroutine. There are alternatives, however, which can be used even if there is no analytic form of the PES available, *i.e.*, the PES is only known on a grid. When computing the matrix representation of the complex scaled potential one might scale the basis functions instead of the PES,[113] or one might evaluate the PES at complex coordinate values from the linear combination of PES values at real coordinate values.[114]

Although there exists at least three examples in the literature[113,115,116] which apply the complex scaling method for computation of nuclear motion resonances of polyatomic molecules, at present such calculations are mainly carried out using the CAP method.[94,95,96,97,98] Therefore, the motivation is quite natural to apply complex scaling for nuclear motion resonance computations within the framework of D^{2}FOPI. In order to achieve a simple methodology, in which the D^{2}FOPI protocol can be straightforwardly exploited, only

the "conventional" complex scaling is considered in the present thesis. The use of alternative complex scaling methods such as exterior complex scaling could be a beneficial improvement but are left to the future. Based on its rigorous mathematical foundation, results obtained with complex scaling could prove to be a useful tool in verifying CAP results, where experiment is not available.

The answer to which coordinates need to be complex scaled in the Hamiltonian used in the D^{2}FOPI protocol naturally depends on the physical system under consideration. For a system with one dissociation channel, using Jacobi-coordinates is the natural choice with the R_2 Jacobi-coordinate being the dissociation coordinate. In this case only the R_2 coordinate should be scaled; thus, for example, considering vibrational resonances the scaled Hamiltonian of Eq. (1) would be (noting that θ is the scaling parameter and Θ is the bending type coordinate)

$$\hat{H}_\theta = -\frac{1}{2\mu_1}\frac{\partial^2}{\partial R_1^2} - \frac{e^{-2i\theta}}{2\mu_2}\frac{\partial^2}{\partial R_2^2} - \left(\frac{1}{2\mu_1 R_1^2} + \frac{e^{-2i\theta}}{2\mu_2 R_2^2}\right)\left(\frac{\partial^2}{\partial \Theta^2} + \cot\Theta\frac{\partial}{\partial \Theta}\right) + \hat{V}\left(R_1, R_2 e^{i\theta}, \Theta\right)$$

For a system with two or three dissociation channels, both R_1 and R_2 need to be scaled. The evaluation of the potential energy function at complex values can be done quite straightforwardly by rewriting the PES subroutine used by the D^{2}FOPI into complex arithmetic.

Obtaining the matrix representation of the scaled Hamiltonian can be done directly, *i.e.*, the matrix representation of the scaled triatomic Hamiltonian is constructed using a direct-product basis, as prescribed by the D^{2}FOPI protocol. Although due to the efficiency of the D^{2}FOPI method this seems to be a useful route, there are at least two factors which hinder this approach. The first is that the matrix representation of the scaled Hamiltonian leads to a complex symmetric matrix which means that for the computation of the required eigenpairs one must use an iterative eigensolver for complex symmetric matrices, which is in general slower than an iterative eigensolver for real symmetric matrices. The second problem is that since the bound states are square integrable eigenstates of the scaled Hamiltonian, before one can compute the resonance states using an iterative eigensolver, one needs to determine all the bound states of the system. This is highly inefficient as usually iterative eigensolvers tend to slow down dramatically as the required number of eigenpairs to be computed increases. To overcome the second problem, one might try using spectral shift techniques. However, they are hindered in nuclear motion computations by the large matrices with large spectral ranges and dense spectra near dissociation. Based on a series of unsuccessful attempts trying several

iterative eigensolver methods, the use of spectral shift techniques didn't seem to be feasible for the present study.

Another way of obtaining the Hamiltonian matrix when combining complex scaling with D^{2}FOPI could be similar to the method applied when merging D^{2}FOPI with using a CAP. First, by using D^{2}FOPI one computes all the bound states of the unscaled Hamiltonian along with many eigenpairs having "energies above the dissociation limit", *i.e.*:

$$\hat{H}\Psi_k = E_k\Psi_k, \quad k \in \{1,2,...,N\} \tag{44}$$

is solved, with N larger than the number of bound states. Then using a subset of the computed eigenvectors as an orthonormal basis set, one constructs the matrix of the scaled Hamiltonian,

$$\mathbf{H}^{\theta}_{kl} = \left\langle \Psi_k \middle| \hat{S}_\theta \hat{H} \hat{S}^{-1}_\theta \middle| \Psi_l \right\rangle, \tag{45}$$

resulting in a very compact matrix representation. Finally, resonance eigenvalues can be obtained via simple direct diagonalization of the matrix in Eq. (45).

Choosing the second approach for obtaining the matrix representation of the complex scaled Hamiltonian, the D^{2}FOPI program package was extended with a code which uses the D^{2}FOPI eigenpairs as input to construct the matrix representation of the triatomic (ro)vibrational Hamiltonian scaled in the R_1 and/or R_2 stretching type coordinates (as set by the user) and computes its eigenvalues via direct diagonalization.

III.3. Applications

III.3.1. One-dimensional tests

In order to see some textbook-type examples on resonance computations and to have some understanding and comparison on the numerical properties of the CAP and complex scaling methods, one-dimensional tests were carried out. The two model systems considered are described by the Hamiltonians

$$\hat{H}_1 = -\frac{1}{2}\frac{d^2}{dr^2} + V_1(r), \quad V_1(r) = \frac{15}{2}r^2e^{-r}, \quad r \in [0,\infty), \tag{46}$$

where $V_1(r)$ is the well known potential of Bain *et al.*,[117] supporting no bound states but a variety of resonance states, and

$$\hat{H}_2 = -\frac{1}{2}\frac{d^2}{dr^2} + V_2(r), \quad V_2(r) = 75\left(1-e^{-2(r-2)}\right)^2 - 75 + \frac{200}{r^2}, \quad r \in [0,\infty), \tag{47}$$

which can be thought of as the Hamiltonian of a Morse-oscillator having a centrifugal barrier term supporting shape resonances. Pictorial representations of the $V_1(r)$ and $V_2(r)$ potentials are given in Fig. 9.

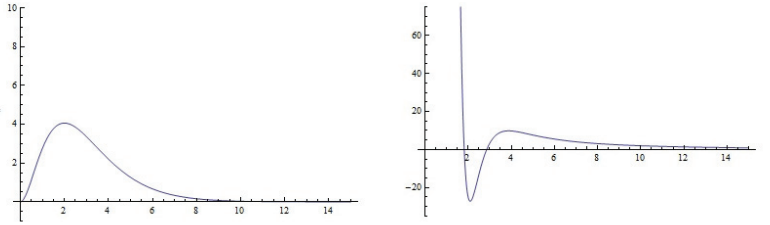

(a) (b)

Figure 9. Pictorial representation of the one-dimensional potentials a) $V_1(r)=\frac{15}{2}r^2e^{-r}$ and b) $V_2(r)=75\left(1-e^{-2(r-2)}\right)^2-75+\frac{200}{r^2}$

When using the CAP method to compute resonances, a simple quadratic absorbing potential of the form

$$W(r)=\begin{cases}0 & , \quad \text{if} \quad r\le r_s\\ -i\eta\left(r-r_s\right)^2, & \text{if} \quad r>r_s\end{cases}$$

was chosen where η is the CAP strength and r_s is the value where the CAP "turns on". Different CAP functions were constructed by setting r_s to 4, 5, 6, or 7. For constructing the eigenvalue trajectories, while η was changed between $\eta_{\min}=0.01$ and $\eta_{\max}=1.00$, or between $\eta_{\min}=0.01$ and $\eta_{\max}=1.50$ in $N_\eta=200$ steps. Following the literature,[92] η was set in the kth step as $\eta_k=\eta_{\min}-1+exp\left[\frac{\ln\left(\eta_{\max}-\eta_{\min}+1\right)}{\left(N_\eta-1\right)}\left(k-1\right)\right]$. It is noted that setting the η values as $\eta_k=\eta_{\min}+\ln\left[1+\frac{\exp\left(\eta_{\max}-\eta_{\min}\right)-1}{\left(N_\eta-1\right)}\left(k-1\right)\right]$ and as $\eta_k=\eta_{\min}+\frac{\eta_{\max}-\eta_{\min}}{N_\eta-1}\left(k-1\right)$ were also tested, but showed to be less effective for finding resonance cusps. Cusp detection followed the protocol described in the end of section III.2.2. setting the energy threshold to 0.01. Cusps were marked as potential resonance eigenvalues if for at least 25% of the

different CAP functions provided a cusp in the same position, *i.e.*, within the distance of the 0.01 energy threshold.

In the case of computing resonances in the framework of the complex scaling method, the scaled 1-D Hamiltonians have the form

$$\hat{S}_\theta \hat{H}_k \hat{S}_\theta^{-1} = -\frac{e^{-2i\theta}}{2}\frac{d^2}{dr^2} + V_k(re^{i\theta}), \quad k \in \{1,2\}, \quad r \in [0,\infty)$$

The scaling parameter θ was set to 0.3 for $k=1$ and was changed between 0.1 and 0.2 for $k=2$ in order to see how basis set convergence is affected by changing the value of θ. Resonance positions were identified by visually interpreting the spectra.

The matrix representation of the 1-D CAP modified Hamiltonians and complex scaled 1-D Hamiltonians were obtained using spherical-oscillator DVR basis functions (for details see Sec. IV.1 in Ref. 5) with parameters $\alpha = 0$ and $R^{\max} = 15$ which means that all the DVR quadrature points are between $r=0$ and $r=15$. Integrals of the differential operator matrix elements were calculated analytically[5] and transformed to the DVR via the transformation method,[6] while the potential and CAP matrices are diagonal in the DVR with the diagonal elements being the functional values of the PES and the CAP, respectively, at the DVR grid points.

The summary of the computed results on the 1-D Hamiltonians of Eq. (46) and Eq. (47) using the complex coordinate method are given in Tables 6 and 7, respectively. Pictorial representation of the results is given in Figures 10 and 11. In Table 7 one can see that by increasing the value of the scaling parameter, basis set convergence tends to slow down. However, if basis set convergence is fully met, bound state and resonance eigenvalues are independent from the value of the scaling parameter. Convergence of the imaginary part of the eigenvalues seems to be slower than that of the real part. An interesting feature observed is that when θ = 0.10, the fourth eigenvalue (second resonance state) seems to converge to a false value, compared to the consistent results of the θ = 0.15 and θ = 0.20 cases. Looking at Figure 11, one can see that the θ = 0.10 choice is "barely" enough for the second resonance state to "become visible", which gives rise to perturbations in the close-lying rotated continuum. Most probably this perturbation is responsible also for the ill convergence of the second resonance state in the θ = 0.10 case. Naturally, the perturbation vanishes as θ is increased, as can be seen in Figure 11. The observation of the perturbative behavior implies that resonance positions obtained from complex scaled Hamiltonians should be treated with

caution, if they are near the rotated continua, as this may lead to inaccurate eigenvalues, despite basis set convergence.

The computed results on the 1-D Hamiltonians using the CAP method are summarized in Table 8. Figure 12 presents some selected eigenvalue trajectories obtained in the CAP method. As Table 8 demonstrates, the CAP method seems to work better for narrow resonances (small Γ), as it only found the first two resonances of the Hamiltonian of Eq. (46), although this feature probably depends on the CAP used. Also, the CAP method might provide unphysical eigenvalues (see results not in bold in Table 8), although when using different CAP functions, the unphysical eigenvalues are usually detected in less cases than the physical ones. A promising result is that the second resonance of the Hamiltonian of Eq. (47), with $E = 11.047$ and $\Gamma = 2.8938$, was obtained in the CAP method with a reasonable accuracy of $E = 11.043$ and $\Gamma = 2.860$ when using 100 basis functions, whereas using the same basis and $\theta = 0.15$ in the complex scaling method resulted in the less accurate values of $E = 11.071$ and $\Gamma = 2.7970$. This implies that the CAP method in some cases might provide accurate eigenvalues with somewhat less computational effort than the complex scaling method.

To sum up, based on the 1-D problems considered here the complex scaling method seems to be more rigorous and reliable with a straightforward usage, while the CAP method might be computationally more efficient.

Table 6. Resonance energies (E) and corresponding inverse lifetime parameters (Γ) of the Hamiltonian of Eq. (46) obtained using the complex coordinate method, computed using different size basis sets (N) and the scaling parameter $\theta = 0.55$.

$N = 40$		$N = 100$		$N = 120$	
E	Γ	E	Γ	E	Γ
3.426	0.01263	3.426	0.01277	3.426	0.01277
4.835	1.11779	4.835	1.11788	4.835	1.11788
5.055	5.97358	5.062	5.96927	5.064	5.96897
5.277	3.38885	5.277	3.38905	5.277	3.38905

Table 7. Resonance and bound state energies (E) and corresponding inverse lifetime parameters (Γ) of the Hamiltonian of Eq. (47) obtained using the complex coordinate method, computed using different size basis sets (N) and scaling parameter (θ) values.

θ = 0.00	N = 60		N = 80					
	E	Γ	E	Γ				
	-17.968	0.000000	-17.967	0.000000				
	-2.920	0.000000	-2.928	0.000000				
θ = 0.10	N =100		N =120		N =140		N =160	
	E	Γ	E	Γ	E	Γ	E	Γ
	-17.967	-0.000113	-17.967	0.000000	-17.967	0.000000	-17.967	0.000000
	-2.928	-0.000943	-2.928	0.000000	-2.928	0.000000	-2.928	0.000000
	7.152	-0.000425	7.152	0.001336	7.152	0.001335	7.152	0.001335
	11.070	2.8657	11.073	2.8798	11.075	2.8942	11.076	2.9080
θ = 0.15	N =100		N =120		N =140		N =160	
	E	Γ	E	Γ	E	Γ	E	Γ
	-17.973	-0.005817	-17.967	-0.000116	-17.967	0.000000	-17.967	0.000000
	-2.967	-0.011821	-2.928	-0.000829	-2.928	0.000000	-2.928	0.000000
	7.093	-0.073925	7.152	-0.000184	7.152	0.001342	7.152	0.001335
	11.071	2.7970	11.048	2.8938	11.047	2.8938	11.047	2.8938
θ = 0.20	N =100		N =120		N =140		N =160	
	E	Γ	E	Γ	E	Γ	E	Γ
	-18.133	1.168860	-17.978	0.008203	-17.967	0.000291	-17.967	0.000000
	-5.818	1.191158	-2.996	-0.019021	-2.928	-0.001694	-2.928	0.000000
	4.488	-3.93038	7.041	0.11997	7.153	0.00147	7.152	0.00136
	11.541	-0.9449	11.082	2.7104	11.048	2.8948	11.047	2.8938

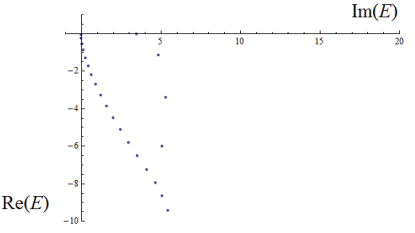

Figure 10. Eigenvalues of the 1-D Hamiltonian of Eq. (46) complex scaled by $\theta = 0.55$, computed with 120 basis functions.

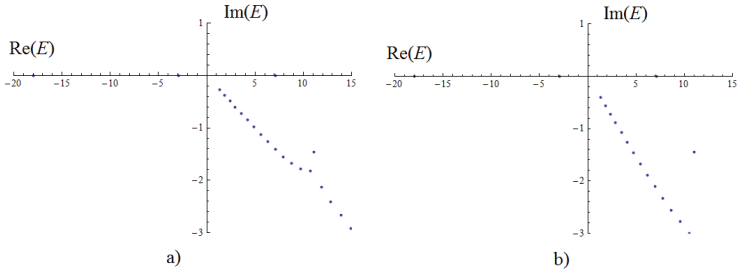

Figure 11. Eigenvalues of the 1-D Hamiltonian of Eq. (47) when complex scaled with a) θ = 0.10 or b) θ = 0.15, obtained using 160 basis functions.

Table 8. Computed energies (E), corresponding widths (Γ) obtained for the one-dimensional test problems using the CAP method. The percentage of the given states being identified with respect to all CAP calculations is also given (%). Results validated by the complex scaling method are in bold (see Tables 6 and 7).

For Hamiltonian of Eq. (47)						For Hamiltonian of Eq. (46)					
N = 80			N = 100			N = 50			N = 80		
E	Γ	%	E	Γ	%	E	Γ	%	E	Γ	%
-17.967	**0.000000**	**87.5**	**-17.967**	**0.000000**	**87.5**	**3.426**	**0.0256**	**100**	**3.426**	**0.0254**	**100**
7.152	**0.000960**	**87.5**	**7.152**	**0.001304**	**100**				**4.828**	**2.164**	**25**
9.313	6.260	25	9.308	6.332	25				4.866	1.986	25
			9.324	5.250	25				4.894	2.002	25
9.359	5.088	25	9.358	5.084	25				5.909	2.980	25
9.378	4.438	25	9.380	4.444	25						
11.037	**2.864**	**37.5**	**11.043**	**2.860**	**75**						
11.569	12.840	25									
			11.651	11.504	25						
11.672	11.808	25	11.673	11.796	25						

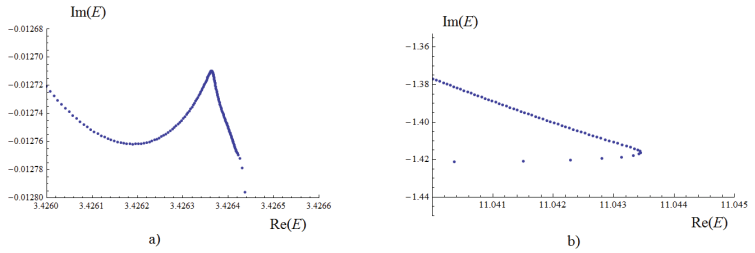

Figure 12. Selected eigenvalue trajectories in the CAP method for the 1-D Hamiltonian of a) Eq. (46) and b) Eq. (47), obtained with using a) 50 and b) 80 basis functions and parameters a) $\eta_{\max} = 1.50,\ r_s = 6$ and b) $\eta_{\max} = 1.50,\ r_s = 4$.

III.3.2. Resonance states of H_2O

As already detailed in the section II.1.4.1., a global PES for the water molecule designed to give correct asymptotic behavior became available only recently. Beyond making it possible to compute nearly all bound states for the system, such a PES which is fairly accurate also in the asymptotic regions and gives the opportunity for the computation of quasi-bound (resonance) states. Based on the PES developed in Ref. 30, Zobov *et. al.*[101] have performed computations using the CAP method for identifying vibrational Feshbach-resonance states and $J = 2$ rovibrational shape-resonance states of the water molecule. Results were compared to the experimental values of Ref. 3. During the comparison with experiment, all theoretical energy values above dissociation were shifted by 38 cm^{-1}, to account for discrepancies in the PES. This was performed as the PES shows, taking into account the zero-point vibrational energy of H_2O and OH, a dissociation energy of D_0=41108 cm^{-1}, which is 38 cm^{-1} lower than the experimental value of 41145±0.15 cm^{-1}. Resonance wave functions, although damped by the CAP, were considered to have similar structure to the bound-state wave functions with energies just below dissociation, *i.e.*, they were considered to be localized in the asymptotic region of the PES, hence the energy shift. Although some features of the experimental spectra were reconstructed, energy differences often reached a few tens of cm^{-1}.

As a test computation for the codes developed on the complex scaling method based on the D^2FOPI protocol, as described in section III.2.4., reproduction and validation of the theoretical nuclear motion results of Zobov *et. al.*[101] was attempted for the vibrational

Feshbach-resonances; naturally, based on the same PES. For discussing $J = 0$ vibrational resonances, one may use the point group instead of the molecular symmetry group, which for H_2O is C_{2v}, which can be exploited in the D^{2}FOPI algorithm, by sorting basis functions into odd and even symmetry blocks. Only odd symmetry states were measured experimentally,[3] thus only those are considered here. In order to have knowledge on the convergence of the obtained resonance states with respect to the basis set size, three sets of D^{2}FOPI computations (see Eq. (44)) were used to obtain eigenvectors for constructing the matrix representation of the scaled Hamiltonian of Eq. (45). The three sets were obtained using (75,95,50), (85,105,50) and (95,115,55) vibrational basis sets, respectively, whereby (n_1,n_2,n_p) means n_1 and n_2 PO spherical-DVR functions (with 400 primitive spherical functions) for the two distance-type and n_p odd parity Legendre basis functions for the angle-type coordinates. Following the notation of Ref. 5, the spherical oscillator basis functions of the R_1 and R_2 coordinates had parameters $R_1^{\max} = 19.0$ bohr, $R_2^{\max} = 11.0$ bohr in the first set, $R_1^{\max} = 20.0$ bohr, $R_2^{\max} =$ 12.0 bohr in the second set, and $R_1^{\max} = 20.5$ bohr, $R_2^{\max} = 12.5$ bohr in the third set. From the three sets, 700, 850 and 900 eigenvectors were taken to construct the scaled Hamiltonian matrix of Eq. (45), respectively. It is noted, that the number of bound odd symmetry states for H_2O is around 525. To obtain the eigenvalue trajectories, the scaling parameter θ was changed between 0.000075 and 0.0030 in thirteen steps, the resonance cusps were identified by visual inspection.

One might see from Figure 13 which shows eigenvalue trajectories on the complex plane computed with the third and largest basis set, that the qualitative picture obtained from the plots is as expected, the bound state eigenvalues are on the real axis, the rotating continua appears above the dissociation energy rotated by an angle of 2θ for a given θ value, and also the resonance states can be observed as cusps on some of the trajectories, as derived in Ref. 112.

Figure 13. Eigenvalues trajectories for the H_2O molecule obtained by diagonalizing the complex scaled Hamiltonian with different θ scaling parameter values. Energy values include Zero-point vibrational energy.

In Table 9 vibrational Feshbach-resonances of the water molecule are presented. Experimental and theoretical values computed with the CAP method (including shifting) and their assignment are taken from Ref. 101, while theoretical values computed with complex scaling and their convergence with respect to basis set size are from the present work. Assignment of the results from complex scaling was done by simply matching energies with experimental values. The remarkable surprise which can be seen in Table 9 is that the resonance energies obtained with complex scaling reproduce the experimental values with considerable accuracy, despite the fact that no energy shifting was applied.

Driven by the numbers of Table 9, comparison of the theoretical results without shifting the energies obtained with the CAP method is summarized in Table 10. For resonance eigenvalues obtained with both methods, calculations show good agreement as far as energy is concerned. The inverse lifetime parameter Γ seems to converge much more slowly than the energy; therefore, they are not taken into account when associating the eigenvalues computed with each other in the two methods. There are resonance states, however, which are obtained with only one of the computational methods. It is not surprising to have some results only determined with complex scaling, since the CAP method is not guaranteed to identify "all" resonance states, as already seen for example in Ref. 113. As to the eigenvalues computed only by the CAP method, they have large Γ parameters (thus, short lifetime), so they remain "hidden" in the range of θ used in the complex scaled computations.

Based on Table 10 one may arrive to the conclusion that the energy shifting used in Ref. 101 was unnecessary for the $J = 0$ Feshbach-resonances and therefore the resulting assignments are false. Recent discussions with the authors of Ref. 101 led to further processing of experimental data and the comparison of the experimental energy levels with theoretical values computed with both CAP and complex scaling methods. So far it seems that for odd symmetry Feshbach-resonance states, experiment and theory are in good agreement, even without any energy shifting.

A simple qualitative explanation for why the computed Feshbach-resonances do not need the energy shifting may lie in the very nature of this type of resonances. Feshbach-resonances arise when the system has enough energy to dissociate; however, this energy is localized in nondissociative vibrational modes. For the water molecule, the bending mode is such a nondissociative motion. If for a given Feshbach-resonance state of water, a significant portion of the energy is stored in the bending mode, this leads to less energy in the

dissociative antisymmetric stretching mode, which in turn means that the wave function is less delocalized in the dissociatve coordinate. Therefore, the inaccuracies in the PES which are responsible for the error in the dissociation energy, are not sampled dominantly for Feshbach-resonance states, since they are restricted to the asymptotic regions of the dissociation coordinate. Naturally, this qualitative explanation needs to be investigated more rigorously, for example by plotting wave functions or computing internal coordinate expectation values.

Table 9. Feshbach-resonance eigenvalues of the water molecule, obtained from measurement (Exp) or computation by using complex absorbing potentials (CAP) or complex scaling (CC). Energies and inverse lifetime parameters (Γ) are given in cm^{-1}.

Exp[a]		CAP [a]		CC[b]		CC conv.[c]	
Energy	Γ	Energy	Γ	Energy	Γ	Energy	Γ
41173.68	0.21	41157.7	0.01	41175.25	<0.001	-0.090	<0.001
41204.74	0.22	41178.5	2.03	41206.58	0.002	4.489	-0.242
41221.24	1	41213.3	0.002	41219.02	0.35	-	-
41226.07	0.42	41244.3	0.33	41224.58	0.012	0.217	-0.020
41264.57	0.09	41262.4	0.3	41259.49	0.68	-	-
41268.17	0.36	41295.8	0.03	41268.79	0.004	0.784	-0.091
41296.78	0.52	41307.0	0.12	41287.84	0.48	1.118	-0.092
41310.77	2.4	41313.1	20.14	41307.44	1.276	-3.979	0.469

[a]Results are taken from Ref. 101
[b]Values were obtained using the (95 115 55) basis set.
[c]Convergence is with respect to results obtained with the (85 105 50) basis set, missing convergence values indicate that those resonances were only identified using the largest (95 115 55) basis set.

Table 10. Feshbach-resonance eigenvalues of the water molecule computed with either a complex absorbing potential (CAP) or the complex scaling method (CC). Energies and inverse lifetime parameters (Γ) are given in cm^{-1}.

CAP[a]		CC[b]		CC conv.[c]	
Energy	Γ	Energy	Γ	Energy	Γ
-	-	41111.20	<0.001	-0.014	<0.001
41119.69	0.010	41113.56	<0.001	0.037	-0.002
41140.49	2.030	-	-	-	-
41175.29	0.002	41175.25	<0.001	-0.090	<0.001
41206.29	0.330	41206.58	0.002	4.49	-0.242
-	-	41219.02	0.354	-	-
41224.39	0.300	41224.58	0.012	0.22	-0.020
41257.79	0.030	41259.49	0.676	-	-
41268.99	0.120	41268.79	0.004	0.78	-0.091
-	-	41287.84	0.480	1.12	-0.092
-	-	41307.44	1.276	-3.98	0.469
41275.09	20.140	-	-	-	-

[a]Results are taken from Ref. 101
[b]Values were obtained using the (95 115 55) basis set.
[c]Convergence is with respect to results obtained with the (85 105 50) basis set, missing convergence values indicate that those resonances were only identified using the largest (95 115 55) basis set.

III.3.3. Resonance states of H_3^+

Although it is one of the simplest polyatomic molecules, even after 30 years, and despite the enormous advances in computers and experimental methods, the H_3^+ spectrum at highly excited regions is neither fully accessed experimentally nor fully described theoretically. For example, the near-dissociation spectrum of H_3^+ reported by Carrington *et al.*[1,2] is still unassigned and poorly understood almost 30 years after it was recorded. Achieving the accuracy with theoretical methods which could be used to reproduce and assign the Carrington lines seems to be beyond the limit of our capabilities at present. Neverheless, this is a valuable goal which fuels methodological developments.

Computation of the $J = 0$ resonances of H_3^+ was attempted using both the CAP method and the complex scaling method based on the D^2FOPI protocol, as described in sections III.2.2. and III.2.4., respectively. For the bound state computations the PPKT2 PES[118] was used, which is known for having a well described asymptotic behavior. This also makes

comparison with previous results[98] straightforward. For discussing $J = 0$ vibrational resonances, one may use the point group instead of the molecular symmetry group, which for H_3^+ is D_{3h}. From this group, however, D^{2}FOPI can only exploit the symmetry of the C_{2v} subgroup, and divide the computations into odd and even symmetry blocks. Only the case of even symmetry is considered in the following.

The basis set used in the D^{2}FOPI computations for obtaining the 1000 initial eigenvectors (see Eqs. (30) and (44), for the CAP and complex scaling methods, respectively) was the vibrational basis set of (120,120,51), whereby (n_1,n_2,n_p) means n_1 and n_2 PO spherical-DVR functions (with 600 primitive spherical functions) for the two distance-type and n_p even parity Legendre basis functions for the angle-type coordinates. Following the notation of Ref. 5, the spherical oscillator basis functions of the R_1 and R_2 coordinates had parameters $R_1^{\max} = R_2^{\max} = 22.0$ bohr. It is noted, that this basis set used for constructing the initial eigenvectors gives the 688 even symmetry bound states of H_3^+ within 1 cm^{-1} convergence.[5] For constructing the complex symmetric matrix representation of the Hamiltonians in the CAP and complex scaling methods (see Eqs. (31) and (45), respectively), the initial eigenvectors numbering from 500-995 and from 1-990 were used, respectively, whereby 1 represents the ground state and numbering is in the order of increasing energy. Including eigenvectors only from 500 when using the CAP method is based on the observation of Silva *et al.*, that further inclusion of bound states does not seem to change the resonance positions.[98]

When using the CAP method to compute resonances, the absorbing potential in Eq. (31) was chosen to have a form

$$W(R_1, R_2) = w(R_1) + w(R_2),$$

where

$$w(R) = \begin{cases} 0 & , \quad \text{if} \quad R \le R_s \\ (R - R_s)^2 & , \quad \text{if} \quad R > R_s \end{cases},$$

and R_s is the value where the CAP "turns on". Different CAP functions were constructed by setting R_s to 13, 15 or 17 bohr for constructing the eigenvalue trajectories, while the CAP strength η of Eq. (31) was changed between $\eta_{\min} = 0.001$ and $\eta_{\max} = 0.25,\ 0.50,\ 0.75,\ 1.00$ or 1.25 in $N_\eta = 500$ steps. Following the literature,[92] η was set in the kth step by $\eta_k = \eta_{\min} - 1 + exp\left[\frac{\ln(\eta_{\max} - \eta_{\min} + 1)}{(N_\eta - 1)}(k-1)\right]$. Resonance positions were identified by the

automatic procedure described in the end of section III.2.2. setting the energy threshold to 1 cm^{-1}, and the inverse lifetime parameter tolerance to 50%. Cusps were associated with resonance eigenvalues if for at least 67% of the different CAP functions provided a cusp in the same position, *i.e.*, within the 1 cm^{-1} energy threshold and having an inverse lifetime parameter agreeing within 50% tolerance.

When using the complex scaling method, the scaling parameter θ was changed between 0.0000625 and 0.0045 in eleven steps to obtain the eigenvalue trajectories, which were interpreted by visual inspection. Computation of the eigenvalue trajectories required a few days CPU time for both the CAP and complex scaling methods.

Table 11 presents the resonances identified up to around 1000 cm^{-1} beyond the first dissociation limit, obtained in the CAP and complex scaling methods along with the CAP results of Silva *et al.*[98], which were obtained with a larger basis set than used for present results. It is clear from Table 11 that many of the resonance eigenvalues computed with the complex scaling method are unconverged, as the Γ inverse lifetime parameters are negative for some of them. These are unphysical values which seem to occur for states where Γ is small enough in absolute value to become negative upon including basis set error. Nonetheless, concerning energy, the majority of the results of Ref. 98 are reproduced with a number of additional resonances identified. The resonances not reproduced by the complex scaling method are probably missing due to the lack of basis set convergence, or they might also be unphysical detections in the CAP method originating from the perturbation of the CAP used. As for the CAP results of the present work, the lower-energy resonances seem to have a systematic overestimation of Γ, compared to their counterparts computed with complex scaling. Also, many of the lower energy resonances are missing. There are quite a few states obtained in the higher-energy regions, which are not identified with complex scaling and are not present in Ref. 98., these are probably unphysical detections.

To sum up, complex scaling seems to work very well, as it reproduces much of previous results and also gives additional resonances, but computations need to be improved by increasing basis set size. The CAP method of present study does not seem to perform very well, as it seems to miss many physical resonances and identify many unphysical ones. Most likely the CAP method could be improved by increasing basis set size, and probably even more so by utilizing more suitable CAP functions instead of the simple quadratic one used in this study.

Table 11. Feshbach-resonance eigenvalues of the H_3^+ molecule taken from Ref. 98 (CAP, Silva *et al.*), or computed using a complex absorbing potential (CAP, this work) or the complex scaling method (CC). Energies and inverse lifetime parameters (Γ) are given in cm^{-1}.

CAP, Silva *et al.*		CAP, this work		CC		CAP, Silva *et al.*		CAP, this work		CC	
Energy	Γ	Energy	Γ	Energy	Γ	Energy	Γ	Energy	Γ	Energy	Γ
34926.61	0.04			34925.88	-0.02			35311.20	3.69		
				34970.56	-0.02			35362.10	7.83	35362.43	0.77
34981.05	0.10			34980.64	-0.006			35368.60	4.78	35375.68	1.80
35012.92	0.003			35009.96	-0.10	35384.23	0.004				
35029.60	0.06			35026.29	0.18			35467.30	2.95		
				35048.28	-0.01			35501.40	1.05		
		35049.10	0.90	35046.27	0.08			35528.70	1.70	35525.91	0.76
35058.82	0.09					35564.58	0.07	35561.50	7.66		
				35072.01	0.07						
35107.54	0.01			35098.75	0.12						
35116.40	0.08			35123.25	0.32			35570.20	14.98		
35153.25	0.00	35150.10	1.67	35149.24	0.26			35576.50	4.96		
				35186.84	1.75			35593.60	19.90		
35190.70	0.02	35190.50	0.46	35187.71	0.46			35602.10	7.20		
35209.69	0.02							35603.80	6.97	35604.97	2.06
				35241.04	1.11			35609.80	20.33		
35243.55	0.09	35243.20	1.27	35244.12	0.92			35625.40	0.87	35623.18	0.42
				35250.70	0.30					35688.46	0.20
				35268.49	0.16					35690.91	1.98
				35271.03	0.12					35715.88	0.90
		35286.90	3.51	35283.81	0.90					35798.69	0.82
		35290.00	3.28							35799.79	0.73
				35302.24	1.51	35822.80	0.08			35824.49	4.62

IV. Summary

The main goal of my PhD work, covered in this thesis, was to develop an efficient variational algorithm and computer code for computing accurate (ro)vibrational resonance states. To achieve this goal requires the availability of an accurate global potential energy surface (PES) of the molecule under investigation and an algorithm which is capable of determining converged bound (ro)vibrational states up to dissociation. The requirement on the PES narrowed the work to triatomic molecules, as global accurate PESs are not available for molecules with more than three atoms at present. Furthermore, to compute resonance states for molecules containing more than three atoms is also extremely challenging.

To have an algorithm and computer code for the accurate variational computation of bound rovibrational states, the D^{2}FOPI protocol, originally developed for vibrational computations was extended to allow the execution of variational rovibrational computations. The rovibrational Hamiltonians employed in the new D^{2}FOPI code are based on the R_1- and bisector embeddings. I successfully applied the extended D^{2}FOPI code computing rovibrational states for the $H_2{}^{16}O$, H_3^+, H_2D^+, and D_2H^+ molecules.

As much of our understanding of high-resolution molecular spectra is based on approximate quantum numbers, I extended the D^{2}FOPI program package with a code computing approximate quantum numbers by utilizing the rigid rotor decomposition (RRD) scheme. Using this code, the embedding dependence and the range of applicability of the RRD scheme with respect to energy and rotational excitation was investigated. I also used the code to validate previously assigned quantum labels for the H_2D^+ and D_2H^+ molecules.

The singular operator term r^{-2} with $r \in [0,\infty)$ often arises in Hamiltonians utilizing internal coordinates, for example in the Hamiltonian used by the D^{2}FOPI protocol. Therefore, the numerical behavior of such terms when applying the diagonal DVR approximation on them was investigated in some detail. The numerical results obtained show that the unexpected applicability of the diagonal DVR approximation for singular operator terms can be traced back to the fact that although within this approximation the matrix elements of the singular operator terms are computed with huge relative error, the eigenvalues are reproduced with surprisingly good accuracy.

After producing an efficient code for the computation of a large number of bound states, I extended the D^{2}FOPI package with two codes for computing (ro)vibrational resonances. These codes are based either on using a complex absorbing potential (CAP) or on the complex scaling method. Of the two techniques the latter received more attention during

this work, as using complex scaling to compute nuclear motion resonances is not a popular choice. The algorithms are based on using a compact basis set of eigenvectors previously computed by the D^2FOPI protocol. Resonance eigenvalues are obtained by identifying cusps in the eigenvalue trajectories, which is automated for the CAP method. As test systems, the H_2O and H_3^+ molecules were chosen, as they are triatomic systems of particular interest and global, accurate PESs are available for them. The complex scaling algorithm proved to be useful in validating previously computed Feshbach-resonances of the H_2O molecule and identifying possible missassignments. For the H_3^+ molecule, the complex scaling method is in good agreement with previous results from the literature, and also provided a number of new Feshbach-resonances.

V. Acknowledgements

First of all, I would like to thank Professor Attila G. Császár for being an exceptional supervisor, supporting plenty of interesting and useful work, and always willing to spare his valuable time and energy to help and guide my research. I am truly very grateful to him.

I am also to thank the people in our group, Dr. Edit Mátyus, Dr. Gábor Czakó, Dr. Tibor Furtenbacher and Csaba Fábri for all their valuable help throughout the years, the useful discussions and for their friendship.

I also thank Dr. Viktor Szalay, Dr. György Tarczay and Dr. Gábor Magyarfalvi for their collaboration and the valuable scientific discussions we had.

I owe thanks to Professor Jonathan Tennyson for sparing his time to read through the draft of my thesis and giving his valuable thoughts on the scientific contents and the English language used.

This work could not have been done without the background of a supporting family. Therefore I thank my mother Dr. Gabriella Szép, for all her support and patience along with the discussions on various mathematical topics during the past few years. I also thank my father Dr. Ferenc Szidarovszky for motivating me and for helping with mathematical issues.

All the way through my PhD work I was fortunate to be supported by the patience and love of Alexandra Urbán, for which I am very grateful.

Finally I thank my rock band and the one drop zendo, both being a refuge for the mind after the long days of intense brainwork.

The European Union and the European Social Fund have provided financial support to this research under Grant No. TÁMOP-4.2.1/B-09/1/KMR-2010-0003. The work described was also supported by the Hungarian Scientific Research Fund (OTKA, Grant Nos. K72885 and NK83583).

[1] A. Carrington, J. Buttenshaw, and R. A. Kennedy, *Mol. Phys.*, **45**, 753 (1982).

[2] A. Carrington, I. R. McNab, and Y. D. West, *J. Chem. Phys.*, **98**, 1073 (1993).

[3] M. Grechko, P. Maksyutenko, T. R. Rizzo and O. V. Boyarkin, *J. Chem. Phys.*, **133**, 081103, (2010).

[4] B. T. Sutcliffe, J. Tennyson, *Int. J. Quant. Chem.*, **39**, 183 (1991).

[5] T. Szidarovszky, A. G. Császár, and G. Czakó, *Phys. Chem. Chem. Phys*. **12**, 8373 (2010).

[6] J. C. Light, T. Carrington, *Adv. Chem. Phys.,* **114**, 263 (2000).

[7]C. G. J. Jacobi, *Cr. Hebd. Acad. Sci.,* **15**, 236, (1842).

[8] R. Radau, *Ann. Sci. Ecole Norm. S*, **5**, 311, (1868).

[9] T. Furtenbacher, G. Czakó, B. T. Sutcliffe, A. G. Császár and V. Szalay, *J. Mol. Struct.*, **780-781,** 283, (2006).

[10] J. Tennyson and B. T. Sutcliffe, *Int. J. Quant. Chem.*, **42**, 941 (1992).

[11]R. N. Zare, *Angular Momentum*, Wiley, New York, (1988).

[12]H. Wei and T. Carrington Jr., *J. Chem. Phys.*, **97**, 3031 (1992).

[13]J. Echave and D. C. Clary, *Chem. Phys. Lett.*, **190**, 225 (1992).

[14] V. Szalay, G. Czakó, Á. Nagy, T. Furtenbacher, and A. G. Császár, *J. Chem. Phys.*, **119**, 10512 (2003).

[15]C. Lanczos, *J. Res. Natl. Bur. Stand.,* **45**, 255 (1950).

[16]J. K. Cullum and R. A. Willoughby, *Lanczos Algorithms for Large Symmetric Eigenvalue Computations*, Birkhauser, Boston, (1985).

[17]Y. Saad, *Iterative Methods for Sparse Linear Systems*; Society for Industrial and Applied Mathematics: Philadelphia, PA, (2003).

[18] Bernath PF., *Phys. Chem. Chem. Phys.*, **4**, 1501, (2002).

[19] J. Tennyson, P. F. Bernath, L. R. Brown, A. Campargue, M. R. Carleer, A. G. Császár, R. R. Gamache, J. T. Hodges, A. Jenouvrier, O. V. Naumenko, O. L. Polyansky, L. S. Rothman, R. A. Toth, A. C. Vandaele, N. F. Zobov, L. Daumont, A. Z. Fazliev, T. Furtenbacher, I. F. Gordon, S. N. Mikhailenko, and S. V. Shirin, *J. Quant. Spectr. Rad. Transfer*, **110**, 573, (2009).

[20] J. Tennyson, P. F. Bernath, L. R. Brown, A. Campargue, **A. G. Császár**, L. Daumont, R. R. Gamache, J. T. Hodges, O. V. Naumenko, O. L. Polyansky, L. S. Rothman, R. A. Toth, A. C. Vandaele, N. F. Zobov, S. Fally, A. Z. Fazliev, T. Furtenbacher, I. F. Gordon, S.-M. Hu, S. N. Mikhailenko, and B. Voronin, IUPAC Critical, *J. Quant. Spectr. Rad. Transfer*, **111**, 2160, (2010).

[21] Mussa HY, Tennyson J., *J. Chem. Phys.*, **109**, 10885, (1998).

[22] Gray SK, Goldfield EM., *J. Phys. Chem.*, **105**, 2634, (2001).

[23] Li GH, Guo H., *J. Mol. Spectrosc.*, **210**, 90, (2001).

[24] Callegari A, Theule P, Tolchenov RN, Zobov NF, Polyansky OL, Tennyson J, et al., *Science*, **297**, 993, (2002).

[25] Grechko M, Maksyutenko P, Zobov NF, Shirin SV, Polyansky OL, Rizzo TR, et al., *J. Phys. Chem. A*, **112**, 10539, (2008).

[26] Grechko M, Boyarkin OV, Rizzo TR, Maksyutenko P, Zobov NF, Shirin S, et al., *J. Chem. Phys.*, **131**, 221105, (2009).

[27] Maksyutenko P, Muenter JS, Zobov NF, Shirin SV, Polyansky OL, Rizzo TR, et al., *J. Chem. Phys.*, **126**, 241101, (2007).

[28] Maksyutenko P, Rizzo TR, Boyarkin OV., *J. Chem. Phys.*, **125**, 181101, (2006).

[29] Barber RJ, Miller S, Dello Russo N, Mumma MJ, Tennyson J, Guio P., *Mon. Not. R. Astron. Soc.*, **398**, 1593, (2009).

[30] A. G. Császár, E. Mátyus, T. Szidarovszky, L. Lodi, N. F. Zobov, S. V. Shirin, O. L. Polyansky, and J. Tennyson, *J. Quant. Spectr. Rad. Transfer*, **111**, 1043, (2010).

[31] J. O. Hirschfelder, *J. Chem. Phys.*, **6**, 795 (1938).

[32] C. A. Coulson, *Proc. Cambridge Philos. Soc.*, **31**, 244 (1935).

[33] R. E. Christoffersen, *J. Chem. Phys.*, **41**, 960 (1964).

[34] G. D. Carney and R. N. Porter, *J. Chem. Phys.*, **60**, 4251, (1974).

[35] T. Oka, *Phys. Rev. Lett.*, **45**, 531 (1980).

[36] P. Drossart et al., *Nature (London)*, **340**, 539 (1989).

[37] L. Neale, S. Miller, and J. Tennyson, *Astrophys. J.*, **464**, 516 (1996).

[38] C. P. Morong, J. L. Gottfried, and T. Oka, *J. Mol. Spectrosc.*, **255**, 13 (2009).

[39] M. Pavanello, L. Adamowicz, A. Alijah, N. F. Zobov, I. I. Mizus, O. L. Polyansky, J. Tennyson, T. Szidarovszky, A. G. Csaszar, M. Berg, A. Petrignani, A. Wolf, *Phys. Rev. Lett.*, **108**, 023002, (2012).

[40] M. Pavanello, L. Adamowicz, A. Alijah, N. F. Zobov, I. I. Mizus, O. L. Polyansky, J. Tennyson, T. Szidarovszky, A. G. Csaszar, *J. Chem. Phys.* (2012), in press.

[41] J. Tennyson, P. Barletta, M. A. Kostin, O. L. Polyansky, and N. F. Zobov, *Spectrochimica Acta A,* **58**, 663 (2002).

[42] T. Furtenbacher, A. G. Császár, and J. Tennyson, *J. Mol. Spectrosc.*, **245**, 115 (2007).

[43] R. E. Moss, *Mol. Phys.*, **89**, 195 (1999).

[44] O. L. Polyansky and J. Tennyson, *J. Chem. Phys.*, **110**, 5056 (1999).

[45] A. G. Császár, C. Fábri, T. Szidarovszky, E. Mátyus, T. Furtenbacher, and G. Czakó, *Phys. Chem. Chem. Phys.*, **14**, 1085 (2012).

[46] A. G. Császár and T. Furtenbacher, *J. Mol. Spectrosc.*, **266**, 99 (2011).

[47] E. Mátyus, C. Fábri, T. Szidarovszky, G. Czakó, W. D. Allen, and A. G. Császár, *J. Chem. Phys.*, **133**, 034113 (2010).

[48] C. Eckart, *Phys. Rev.*, **47**, 552 (1935).

[49] A. Y. Dymarsky and K. N. Kudin, *J. Chem. Phys.*, **122**, 124103 (2005).

[50] E. Mátyus, G. Czakó, and A. G. Császár, *J. Chem. Phys.*, **130**, 134112 (2009).

[51] C. Fábri, E. Mátyus, and A. G. Császár, *J. Chem. Phys.*, **134**, 074105 (2011).

[52] H. Wei and T. Carrington Jr., *J. Chem. Phys.*, **107**, 2813 (1997).

[53] S. V. Shirin, O. L. Polyansky, N. F. Zobov, P. Barletta, and J. Tennyson, *J. Chem. Phys.*, **118**, 2124 (2003).

[54] R. J. Barber, J. Tennyson, G. J. Harris, and R. N. Tolchenov, *Mon. Not. R. Astron. Soc.*, **368**, 1087 (2006).

[55] G. Hose and H. S. Taylor, *Phys. Rev. Lett.* **51**, 947, (1983).

[56] M. Hazewinkel, *Encyclopaedia of Mathematics*, Reidel, Kluwer, (1994).

[57] J. E. Marsden and M. J. Hoffman, *Basic Complex Analysis*, New York, Freeman, (1987).

[58]R. Cushman, *Centruum voor Wiskund Inf. Newslett*., **1**, 4 (1983).

[59]L. R. Bates, *J. Appl. Math. Phys.* **42**, 837 (1991).

[60]M. S. Child, T. Weston, and J. Tennyson, *Mol. Phys.*, **96**, 371 (1999).

[61]N. F. Zobov, S. V. Shirin, O. L. Polyansky, J. Tennyson, P.-F. Coheur, P. F. Bernath, M. Carleer, and R. Colin, *Chem. Phys. Lett.*, **414**, 193 (2005).

[62] A. G. Császár, W. D. Allen, and H. F. Schaefer III, *J. Chem. Phys.*, **108**, 9751 (1998).

[63] G. Tarczay, A. G. Császár, W. Klopper, V. Szalay, W. D. Allen, and H. F. Schaefer III, *J. Chem. Phys.*, **110**, 11971 (1999).

[64] E. F. Valeev, W. D. Allen, H. F. Schaefer III, and A. G. Császár, *J. Chem. Phys.*, **114**, 2875 (2001).

[65] P. R. Bunker and P. Jensen, *Molecular Symmetry and Spectroscopy*, NRC, Ottawa, (1998).

[66] L.-Y. Peng, A.F. Starace, *J. Chem. Phys.*, **125**, 154311 (2006).

[67] M. Vincke, L. Malegat, D. Baye, *J. Phys. B*, **26**, 811 (1993).

[68] G. Schiffel, U. Manthe, *Chem. Phys.*, **374**, 118 (2010).

[69] J.R. Henderson, J. Tennyson, B.T. Sutcliffe, *J. Chem. Phys.*, **98**, 7191 (1993).

[70] G. Czakó, T. Furtenbacher, P. Barletta, A.G. Császár, V. Szalay, B.T. Sutcliffe, *Phys. Chem. Chem. Phys.*, **9**, 3407 (2007).

[71] A.V. Meremianin, J.S. Briggs, *Phys. Rep.*, **384**, 121 (2003).

[72] R.G. Littlejohn, M. Reinsch, *Rev. Mod. Phys.*, **69**, 213 (1997).

[73] G. Czakó, V. Szalay, A.G. Császár, T. Furtenbacher, *J. Chem. Phys.*, **122**, 024101 (2005).

[74] M.J. Bramley, J.W. Tromp, T. Carrington Jr, G.C. Corey, *J. Chem. Phys.*, **100**, 6175 (1994).

[75] G. Czakó, V. Szalay, A.G. Császár, *J. Chem. Phys.*, **124**, 014110 (2006).

[76] J.K.G. Watson, *Can. J. Phys.*, **72**, 702 (1994).

[77] M. Hesse, *Phys. Rev. E,* **65**, 046703 (2001).

[78] A.S. Dickinson, P.R. Certain, *J. Chem. Phys.*, **49**, 4209 (1968).

[79] D.O. Harris, G.G. Engerholm, W.D. Gwinn, *J. Chem. Phys.*, **43**, 1515 (1965).

[80] G. Szego, *Orthogonal Polynomials*, Am. Math. Soc. (1939).

[81] R. Schinke, *Photodissociation Dynamics*, Cambridge University Press, Cambridge, (1993).

[82] J. R. Taylor, *Scattering Theory*, Wiley, New York, (1972).

[83] R. E. Wyatt and J. Z. H. Zhang, *Dynamics of Molecules and Chemical Reactions*, Marcel Dekker, New York, (1996).

[84] V. I. Kukulin, V. M. Kasnopolsky and J. Horacek, *Theory of Resonances*, Kluwer, Dordrecht, (1988).

[85] A. Bohm, H. Uncu and S. Komy*, Rep. Math. Phys.*, **64**, 5, (2009).

[86] A.Bohm*, Rep. Math. Phys*., **67**, 279, (2011).

[87] L.D. Landau, E.M. Lifshitz, *Quantum Mechanics*, Pergamon, Oxford (1965).

[88]N. Moiseyev, *Phys. Rep.*, **302**, 211, (1998).

[89]Y.K. Ho, *Phys. Rep. C*, **99**, 1, (1983).

[90]W. P. Reinhardt, *Annu. Rev. Phys. Chem.*, **33**, 223, (1982).

[91] G. Jolicard, C. Leforestier and E. Austin, *J. Chem. Phys.*, **88**, 1026, (1988).

[92] U. V. Riss and H.-D. Meyer, *J. Phys. B: At., Mol. Opt. Phys.*, **26**, 4503, (1993).

[93] J. G. Muga, J. P. Palao, B. Navarro and I. L. Egusquiza, *Phys. Rep.*, **395**, 357, (2004).

[94] S. Skokov, J. M. Bowman and V. A. Mandelshtam, *Phys. Chem. Chem. Phys.*, **1**, 1279, (1999).

[95] B. Poirier and T. Carrington Jr., *J. Chem. Phys.*, **116**, 1215, (2002).

[96] H. Y. Mussa and J. Tennyson, *Chem. Phys. Lett.*, **366**, 449, (2002).

[97] J. C. Tremblay and T. Carrington Jr., *J. Chem. Phys.*, **122**, 244107, (2005).

[98] B. C. Silva, P. Barletta, J. J. Munro and J. Tennyson, *J. Chem. Phys.*, 128, 244312, (2008).

[99] A. Carrington, I. R. McNab and Y. D. West, *Chem. Phys.*, **98**, 1073, (1993).

[100] J. Miyawaki, K. Yamanouchi and S. Tsuchiya, *Chem. Phys.*, **99**, 254, (1993).

[101] N. F. Zobov, S. V. Shirin, L. Lodi, B. C. Silva, J. Tennyson, A. G. Császár and O. L. Polyansky, *Chem. Phys. Lett.*, **507**, 48, (2011).

[102] R. Schinke, *Photodissociation Dynamics*, Cambridge University Press, Cambridge, (1993).

[103] G. S. Whittier and J. C. Light, *J. Chem. Phys.*, **107**, 1816, (1997).

[104] T. P. Grozdanov, V. A. Mandelshtam and H. S. Taylor, *J. Chem.Phys.*, **103**, 7990, (1995).

[105] B. Poirier and J. C. Light, *J. Chem. Phys.*, **114**, 6562, (2001).

[106] T. Slee and R. J. L. Roy, *J. Chem. Phys.*, **99**, 360, (1993).

[107] D. D. Sokolov, *Curvature*, in Hazewinkel, Michiel, *Encyclopedia of Mathematics*, Springer, (2001).

[108] J. Aguilar and J.M. Combes, *Commun. Math. Phys.*, **22**, 269, (1971).

[109] E. Balslev and J.M. Combes, *Commun. Math. Phys.*, **22,** 280, (1971).

[110] B. Simon, *Commun. Math. Phys.*, **27**, 1, (1972).

[111] M. Reed, B. Simon, *Methods of Modern Mathematical Physics, Volume 4, Analysis of Operators*
, Academic Press Inc., (1972).

[112] N. Moiseyev, S. Friedland and P. R. Certain, *J. Chem. Phys.*, **74**, 4739, (1981).

[113]V V. Ryaboy, N. Moiseyev, *J. Chem. Phys.*, **103**, 4061, (1995).

[114] V. A. Mandelshtam and N. Moiseyev, *J. Chem. Phys.*, **104**, 6192, (1996)

[115] V. Ryaboy, N. Moiseyev, V. A. Mandelshtam, and H. S. Taylor, *J. Chem.*
Phys., **101**, 5677 (1994).

[116] S.I.Chu, *J. Chem. Phys.*, **72**, 4772, (1980).

[117] R. A. Bain, J. N. Bardsley, B. R. Junker and C. V. Sukumar, *Phys. B: At. Mol. Phys.*, 7, 2189, (1974).

[118] J. J. Munro, J. Ramanlal, J. Tennyson and H. Y. Mussa, *Mol. Phys.*, **104**, 115, (2006).